The Tokar Gap Jet: Regional Circulation, Diurnal Variability, and Moisture Transport Based on Numerical Simulations

SHANNON R. DAVIS AND LAWRENCE J. PRATT

Physical Oceanography Department, Woods Hole Oceanographic Institution, Woods Hole, Massachusetts

HOUSHUO JIANG

Applied Ocean Physics and Engineering Department, Woods Hole Oceanographic Institution, Woods Hole, Massachusetts

(Manuscript received 11 September 2014, in final form 3 March 2015)

ABSTRACT

The structure, variability, and regional connectivity of the Tokar Gap jet (TGJ) are described using WRF Model analyses and supporting atmospheric datasets from the East African–Red Sea–Arabian Peninsula (EARSAP) region during summer 2008. Sources of the TGJ's unique quasi-diurnal nature and association with atypically high atmospheric moisture transport are traced back to larger-scale atmospheric dynamics influencing its forcing. These include seasonal shifts in the intertropical convergence zone (ITCZ), variability of the monsoon and North African wind regimes, and ties to other orographic flow patterns. Strong modulation of the TGJ by regional processes such as the desert heating cycle, wind convergence at the ITCZ surface front, and the local land–sea breeze cycle are described. Two case studies present the interplay of these influences in detail. The first of these was an ''extreme'' gap wind event on 12 July, in which horizontal velocities in the Tokar Gap exceeded 26 m s^{-1} and the flow from the jet extended the full width of the Red Sea basin. This event coincided with development of a large mesoscale convective complex (MCC) and precipitation at the entrance of the Tokar Gap as well as smaller gaps downstream along the Arabian Peninsula. More typical behavior of the TGJ during the 2008 summer is discussed using a second case study on 19 July. Downwind impact of the TGJ is evaluated using Lagrangian model trajectories and analysis of the lateral moisture fluxes (LMFs) during jet events. These results suggest means by which TGJ contributes to large LMFs and has potential bearing upon Sahelian rainfall and MCC development.

1. Introduction

Circulation in the lower troposphere is greatly influenced by hills and mountains, as well as the gaps and valleys formed between them. Indeed, the term ''gap winds,'' coined by Reed (1931), designates the unique topographically influenced flow pattern that develops in response to constriction of lower atmospheric flow as it passes between elements of elevated topography. These flows are triggered by horizontal pressure gradients across the gap axis, resulting in low-level jetlike flows (10–30+ m s^{-1}) emanating between the topographic elements. While gap winds vary significantly as a function of gap length and geometry, the development and intensity of gap wind flows is largely a function of local synoptic patterns and seasonal variations in the local atmosphere. This is particularly true where gap winds influence coastal regions, as recent research has shown with coastal gap winds (CGWs) contributing significantly to local circulation patterns, extreme weather events, atmospheric transport, and climate-scale processes.

Efforts have begun to illuminate the connections between CGWs, extreme atmospheric events, and regional climate. Hughes and Hall (2010) found anticyclone development over the Great Basin to be the leading mechanism in the onset of gap wind flows and/or Santa Ana winds, particularly during the height of dry surface conditions and severe wildfire outbreaks in Southern California. Bastin et al. (2006) found that a collision between mistral-driven CGWs and the local sea breeze was responsible for lower-atmospheric stagnation and the accumulation of increased boundary layer pollutant levels along the Mediterranean coast of France. Bergamasco

Corresponding author address: Shannon R. Davis, Physical Oceanography Department, Woods Hole Oceanographic Institution, 266 Woods Hole Rd., MS#21, Woods Hole, MA 02543.
E-mail: sdavis@whoi.edu

DOI: 10.1175/JCLI-D-14-00635.1

and Gačić (1996) showed that extreme bora events drive sharp changes in the Ekman dynamics of the Adriatic Sea, and occasionally the reversal of surface ocean currents. Over larger spatial and temporal scales, a series of studies have presented the influence of the Tehuantepec gap and associated Central American CGWs (Papagayo, Panama) on the annual sea surface temperature (SST) cycle. Specifically, the gap winds increase the amplitude of the SST cycle through the generation of eddies and other enhancements of the vertical entrainment process in the ocean (Sun and Yu 2006). This modification significantly impacts the Pacific warm pool and induces a shoaling of the thermocline in the eastern Pacific basin (Xie et al. 2005; Xu et al. 2005). As a result, a feedback loop between ocean and atmosphere is formed, resulting in a suppression and displacement of atmospheric deep convection and rainfall. Climate model simulations and satellite observations suggest that this may be an underlying mechanism for the midsummer drought of Central America (Karnauskas et al. 2013; Romero-Centeno et al. 2007).

More recent efforts have also shown that the southwesterly monsoon winds over East Africa excite similar gap wind jets across the Red Sea (Jiang et al. 2009; Zhai and Bower 2013), leading to formation of wind-driven ocean eddies, enhanced vertical mixing in the ocean, and interannual variability in the Red Sea. The leading CGW in these Red Sea studies is the Tokar Gap jet (TGJ), whose location is shown in Fig. 1.

This gap wind jet has recently emerged as a feature of interest in several other related studies of the East African–Red Sea–Arabian Peninsula (EARSAP) region. While forecasters have been aware of the TGJ for a number of years, it is only through recent studies that many of its characteristics and some of its impacts have come to light. Unlike the well-known Central American gap winds (Tehuantepec and Papagayo), which are episodic in nature (Chelton et al. 2000), the TGJ manifests quasi-regularly throughout the summer season with a (near) diurnal frequency (Jiang et al. 2009). This characteristic contributes to the impact of the TGJ within the regional atmosphere as well as in terms of climate-related atmospheric processes. Hickey and Goudie (2007) identified the Sudanese coast immediately around the Tokar Gap delta as one of two major source regions for Northern Hemisphere dust storms.

Lagrangian model simulations by Viste and Sorteberg (2013a) further showed that topography surrounding the Red Sea shapes regional moisture transport pathways and that the general location of the Tokar Gap (TG) may coincide with a principal route of moisture transport in the EARSAP region, thus tying the TGJ to Sahelian rainfall patterns as well as the development of regional mesoscale convective systems (thunderstorms).

It is the purpose of this study to identify major atmospheric processes that control, or are influenced by, the TGJ and its seasonal and diurnal variability. We will do so through the analysis of high-resolution numerical model simulations, regional observations, and global reanalyses. Specifically, Weather Research and Forecasting (WRF) Model simulations and data analysis are used with a primary focus upon conditions during the summer of 2008. Section 2 of the study presents a description of the model and datasets used in the analysis, accompanied by validation of the model downscaling during this period of study. Section 3 then advances an analysis of the TGJ and associated processes in order to identify the regional factors that control the diurnal variability of the jet. This is achieved through a consideration of global-scale influences on the lower atmospheric flow in the EARSAP region and then in section 4, of interactions with regional-specific processes such as the intertropical convergence zone (ITCZ) surface front migration and the land–sea breeze cycle around the Red Sea. We then describe two case studies (section 5), the first being an extreme event and the second a more typical strong event. The downwind impacts of the TGJ are then evaluated in terms of the latent heat fluxes and lateral moisture fluxes (section 6). To put these fluxes in context, we also calculate the lateral moisture fluxes across other strategic vertical sections over the Red Sea and East Africa highlands. Possible connections with mesoscale convective complex development are then discussed. A final summary, conclusions, and a preview of the second part of this study are advanced in section 7.

2. Data and model descriptions

The Advanced Research Weather Research and Forecasting (WRF-ARW) Model (hereafter ARW) dynamic core version 3.0.1.1 (Skamarock et al. 2008) was used in this study to dynamically downscale the 1° NCEP Global Final Analysis (FNL) to a regional Red Sea subdomain as described in Jiang et al. (2009). The NCEP FNL is generated at 6-hourly intervals using the Global Data Assimilation System (GDAS), which continuously collects observational data from the Global Telecommunications System (GTS), as well as other sources, for its analyses. In the WRF Model simulations/downscaling of this data, the approach of successive integrations with daily reinitializations was employed in WRF Model simulations of spanning 1 December 2007–31 January 2009, with datasets generated at hourly temporal resolution. The subdomain consisted of a 10-km fine-resolution domain nested within a coarser 30-km-resolution grid as presented in Fig. 1. In the vertical, 35 terrain-following eta levels were used with the first grid points ~100–150 m

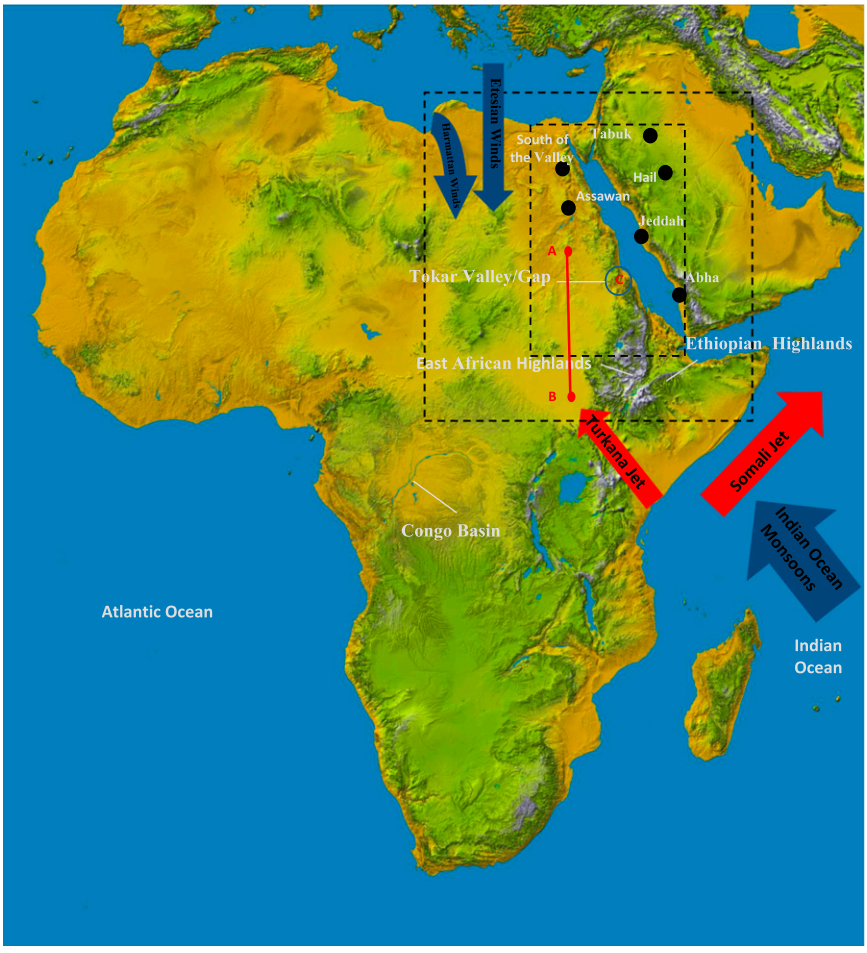

FIG. 1. Primary EARSAP topographic influences in relation to the Tokar Gap as seen in the NASA Shuttle Radar Topography Mission (SRTM) map of Africa. Labeled features include the Ethiopian highlands, the East African highlands, the Great Rift Valley/Turkana valley region, and the Congo basin. The large-scale and high-resolution domains are also indicated (black rectangles), with lower wind patterns of the summertime lower tropospheric circulation across the region (blue arrows) and orographic jets (red arrows). Stations providing atmospheric data for model verification are indicated by black dots and points used to evaluate model profiles and vertical cross sections in the analysis are indicated by red dots and lines.

above the ground level. The NCEP daily data of 0.083° global SST analysis (RTG_SST_HR) (Thiébaux et al. 2003) were used to force the lower boundary of the WRF Model. The Yonsei University (YSU) boundary layer parameterization scheme was employed to accurately render the diurnal variability of the atmospheric boundary layer. A more detailed overview of this year long wind field, including a discussion of the TGJ and wintertime offshore jets in the northern Red Sea, can also be found in Jiang et al. (2009).

Observational soundings made during the study period were used in the validation of the model downscaling (section 3). The specifics of stations and times used are described fully in that section and these data have been made freely available by the Department of Atmospheric Sciences at the University of Wyoming. The National Aeronautics and Space Administration's (NASA's) Modern-Era Retrospective Analysis for Research and Applications (MERRA) data were further used in this study. These data are made available by the Global Modeling and Assimilation Office (GMAO). In particular, reanalyses of mean sea level pressure (SLP), total outgoing longwave radiation (OLR) based on Atmospheric Infrared Sounder (AIRS) measurements, and horizontal wind vectors at 1000- and 500-hPa pressure levels were used.

Lagrangian trajectories were calculated by the NOAA HYSPLIT dispersion model using NCEP reanalysis forcing.

Model vertical velocities were used in these calculations to produce trajectory ensembles of the TGJ inflow and outflow patterns. Trajectories were calculated as ensembles with multiple trajectories initiated from selected starting (ending) locations for forward (backward) paths. Each member of the trajectory ensemble was calculated by offsetting the meteorological data by a fixed grid factor (one meteorological grid point in the horizontal and 0.01 sigma units in the vertical). This results in 27 members for all possible offsets in the x, y, and z directions (see the NOAA HYSPLIT website at http://ready.arl.noaa.gov/READYtransp.php).

3. Validation

Validation of the WRF Model's performance in downscaling has been previously demonstrated in the work of Jiang et al. (2009), in which surface wind speed and heat fluxes were shown to be in close agreement with observations made at an air–sea buoy moored off the Saudi coast, northeast of the TG. Further comparison is now made between selected simulated variables and region-wide observations. Specifically, model parameters were evaluated in relation to radiosonde soundings made at six observation stations in the region as seen in Fig. 1. The selection of observation stations was made based on availability of data and to represent different geographical influences across the EARSAP region. For time convention, we adopt the local standard time (LST) convention, also known as Arabian standard time. These times are equivalent to coordinated universal time (UTC) plus 3 hours (LST = UTC + 3 h).

Jeddah, Saudi Arabia (21.70°N, 39.19°E; 19 m elevation), presented the closest available observations to the Tokar Gap outflow. Like the stations at Abha, Saudi Arabia (18.23°N, 42.65°E; 2093 m elevation), and Aswan, Egypt (23.96°N, 32.78°E; 94 m elevation), observations at Jeddah captured coastal circulation patterns around the Red Sea including sea- and land-breeze regimes. The second Egyptian observation station, South of the Valley (26.20°N, 32.75°E; 96 m elevation), also provided observations of the inflow of the northerly Harmattan and Etesian winds behind the Red Sea Hills. Saudi Arabian stations at Hail (27.43°N, 41.68°E; 1002 m elevation) and Tabuk (28.36°N, 36.5°E; 768 m elevation) further presented observations from the central and northern Arabian Peninsula respectively.

Throughout the period of interest, and over most of the locations, the WRF Model fields accurately represented the vertical atmospheric structure, particularly in the tropospheric region of interest (the lowest 6000 m). This is evident from the profile comparisons presented in Fig. 2. Overall, model values of temperature, water vapor mixing ratio, and wind speed compared well with observations at each of the six regional stations during the case study made on 12 July 2008. Discrepancies such as those seen in the WRF Model–Aswan comparison may have resulted from subgrid-scale processes present in the sounding measurements. Smoothing of the model fields in such circumstances may have also occurred through an overestimate of the friction velocity u^* and resulting overmixing in the lower atmosphere by the YSU parameterization scheme used in the downscaling simulations (Draxl et al. 2014). The highest levels of agreement between balloon and model values appeared in the profiles of temperature. As seen in this particular comparison time and date, model water vapor mixing ratios were slightly higher than observed in the lower atmosphere over Aswan, Abha, and Jeddah while model wind speeds below 6 km were slightly lower than those observed over each of the stations with the exception of Jeddah. Further evaluation of the differences between the model and the regional radiosonde profiles was made over a 10-day period between 4 and 14 July 2008 during which sufficient observations were available for comparison. In this period a root-mean-square error (RMSE) of 1.16 m s^{-1} was determined between the model and sounding wind speeds in the lower 6 km. Corresponding differences in lower tropospheric state variables was small yet discernible, with 1.38°C and 0.85 g kg^{-1} RMSEs calculated for temperature and water vapor mixing ratio respectively, further suggesting that no apparent bias persisted in the model simulation There exists some uncertainty as to whether any soundings used in this comparison were incorporated in the original FNL product forcing the WRF Model simulations.

4. Regional atmospheric influences on the TGJ

The TGJ is a response to synoptic-scale wind forcing regimes. These summertime regimes primarily comprise northerly winds from North Africa and the eastern Mediterranean Sea and the Indian Ocean monsoons from the south. As detailed below, the cycle of the TGJ and its variability are controlled by these wind patterns and also influenced by the local Red Sea land–sea breeze cycle.

a. Background circulation

The geography surrounding the TGJ plays a central role in its occurrence as well as its downwind impacts. At 18°N, 38°E, the Tokar Gap is situated where the easternmost extent of the African Sahel meets the Red Sea. This position coincides with the northernmost reaches of the ITCZ's summer migration. Hence, during summer months, the Tokar Gap lies at a crossroads of influences of the seasonal Indian Ocean monsoon cycle to the south

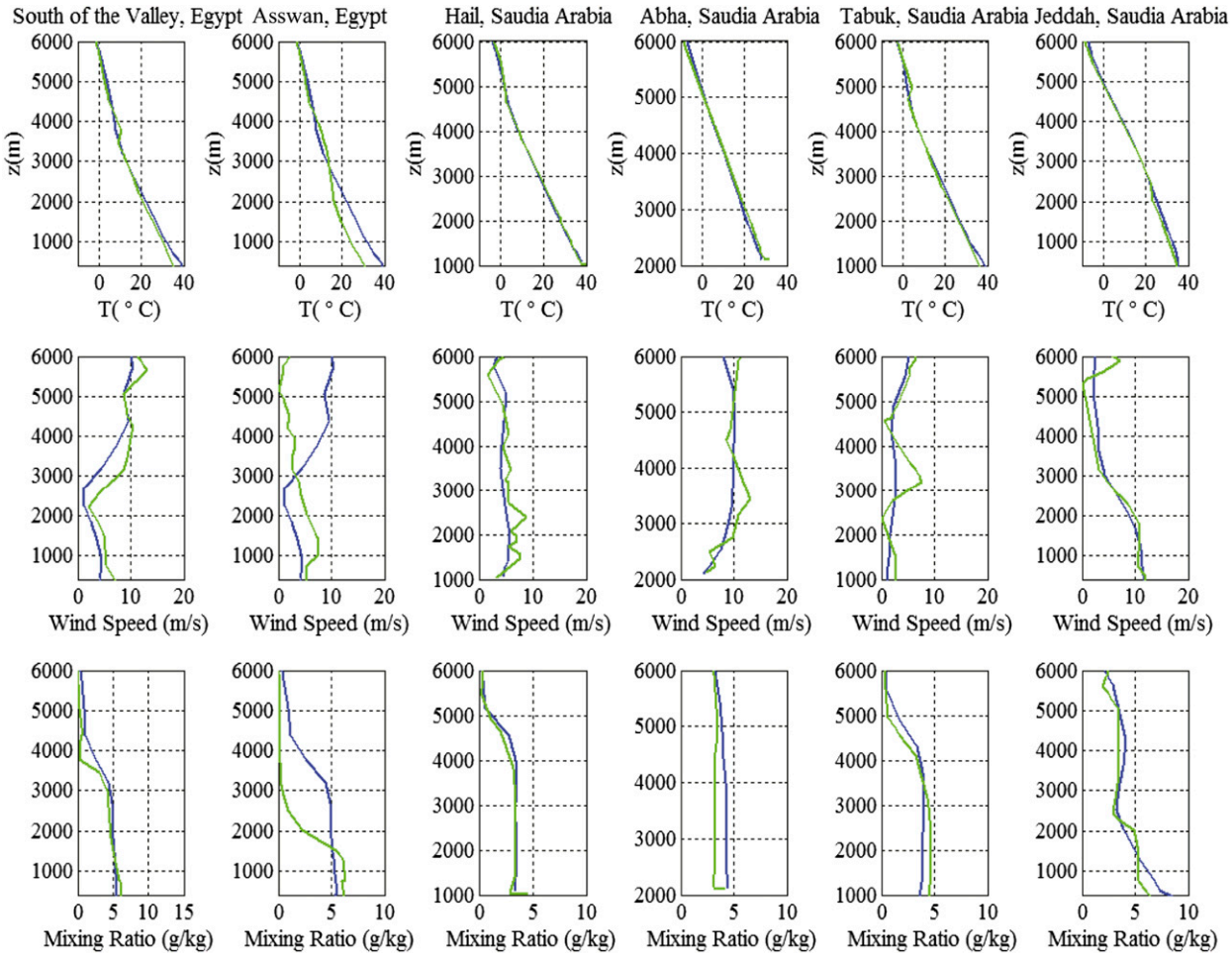

FIG. 2. Shown are profiles of (top) atmospheric temperature, (middle) wind speed, and (bottom) water vapor mixing ratio during the case study of typical gap wind jets made on 19 Jul 2008. Observed values measured at Jeddah, Saudi Arabia (SA); Tabuk, SA; Hail, SA; Abha, SA, South of the Valley, Egypt, and Aswan, Egypt, are marked by green lines while WRF Model values are in blue.

and the seasonal patterns of the Sahara Desert and eastern Mediterranean Sea to the north. Through the analysis of the WRF Model simulations, we suggest (and explore further in sections 4c and 5) that the fluctuation in intensity of the local desert heat low and the position of the ITCZ greatly influence the arrival of the southerly summer monsoon winds at the gap and thus the timing of the TGJ initiation.

The summer monsoon winds are the leading element forcing the Tokar Gap wind jets (Jiang et al. 2009; Zhai and Bower 2013) and arise largely from the differential heating between the Indian Ocean and surrounding landmasses. In this sense they behave as large-scale sea breezes (Chang 2004) with large-scale convection developing across tropical continental regions such as Saharan North Africa and the Tibetan Plateau. Convection results in broad bands of low pressure in the continental lower troposphere, inducing a rapid inflow of cooler moist winds from the Indian Ocean. This process is accompanied by cross-equatorial flow in lower atmospheric layers as well as shifts in the semipermanent pressure centers over the Atlantic and Indian Ocean basins.

Chief among the Southern Hemisphere semipermanent anticyclones influencing the EARSAP region are the Saint Helena high (SHH), an extension of the South Atlantic high pressure system, and the Masacarene high (MSH), a semipermanent high pressure system of the southern Indian Ocean. While both features intensify in boreal summer, the MSH acts in concert with Northern Hemisphere features to drive the southerly summer monsoon winds in the region as described in Webster et al. (1998). Specifically, intensification of the MSH couples with the dissipation of the Siberian high anticyclone (not shown) and the formation of the Asian low and its extension, the monsoon trough, thus providing the necessary pressure gradient for the southerly flow inherent in the monsoon

winds over the EARSAP region. This flow is further enhanced by the westward retreat of the Bermuda–Azores anticyclone and dissipation of its extension, the Sahara high, from its wintertime position over the western North Atlantic during the boreal summer. Increased solar insolation and resulting surface temperatures over the Sahara induces the formation of broad low pressure region stretching across the Sahel from the Atlantic to the Red Sea. Over seasonal time frames, the evolution of this low pressure band is central to the north–south migration of the ITCZ and corresponding monsoon wind regimes (Ramel et al. 2006; Sultan and Janicot 2003). On shorter time scales, the position of the low pressure region along the ITCZ figures prominently in the summertime inflow of lower atmospheric winds to the Tokar Gap.

Over northwest Africa, development of this Sahelian low pressure band accompanies the formation of the seasonal Saharan heat low (SHL) seen in Fig. 3a. Together, these low pressure regions mark the ITCZ, the boundary between the Northern and Southern Hemisphere Hadley cells. The ITCZ is characterized as the zone of lowest pressure in the tropical atmosphere and its surface position is a transitional region between higher and lower rates of net outgoing longwave radiation as seen in Figs. 4a and 4b. Over seasonal time scales, the Hadley cells adjust to the changing angle of solar insolation, resulting in corresponding shifts of the mean position of the ITCZ. In Northern Hemisphere summer, this implies a northward shift of the ITCZ and the drawing of the southeasterly trade winds of the Southern Hemisphere across the equator. A deflection by the Coriolis effect transforms the lower atmospheric winds into southwesterly as they progress into the Northern Hemisphere and eastward across the Indian Ocean between the equator and 15°N (Fig. 3a). Another key summertime feature in the middle-to-upper troposphere is the development of the African equatorial jet (AEJ). This can be seen in the winds at 500 hPa in Fig. 3b.

Figures 5a and 5b present an enhanced view of these large-scale atmospheric influences upon the TG flow as seen through the HYSPLIT model back-trajectories, initiated at 300-m altitude and computed for two strong jet events on 12 and 19 July 2008 (these events are detailed extensively in section 5). In both cases, trajectories entering the gap from the north follow pathways consistent with the Sahelian low pressure region inducing the combined flow of the seasonal Harmattan winds formed over the eastern Sahara and the Etesian winds from the eastern Mediterranean Sea toward the TG. A majority of the southern trajectories meanwhile are largely indicative of the southerly Indian Ocean monsoon winds being channeled inland north of the MSH and through the East African topography toward the western side of the Red Sea Hills. Also apparent are southerly trajectories, which reflect possible contributions from the West African monsoons crossing the continent through the Congo basin and thus inflow from the Atlantic coast under the influence of the SHH. The striking convergence of air parcels from the north and south also provides a clear indication of the ITCZ's central role in the summertime inflow into the Tokar Gap.

b. *Role of the ITCZ*

During the July 2008 period of focus, the diurnal variability of the TGJ can be directly linked to several (not necessarily independent) factors. At the downstream end of the gap, the flow is influenced by the local Red Sea land and sea breeze cycle. Upstream, the TGJ is tied to the intense surface heating cycle across the ITCZ that stretches over the eastern Sahel and Sahara. This heating cycle drives large diurnal variations in sea level pressure (SLP), which in turn control the behavior of the horizontal convergence in the lower atmospheric winds around the ITCZ.

These processes can be seen in the conditions surrounding a 12 July 2008 TGJ event as shown in Fig. 6. In a 36-h time series within the ITCZ (point A in Fig. 1), an out-of-phase relationship between simulated potential temperature and surface pressure (Fig. 6a) was apparent. At point C within the entrance to the Tokar Gap, the temperature–pressure relationship is also largely out of phase (Fig. 6b). Here the temperature–pressure phase lag is influenced by the local Red Sea land–sea breeze cycle (see section 4). In both cases, the diurnal cycle was pronounced, with surface heating increasing over the course of the day and maximum surface temperatures recorded around 1500 LST. Nocturnal cooling contributed to the development of minima nearly 12 h later (~0300 LST).

The regions of most intense daytime surface heating were the Arabian Peninsula and a zonal band centered at the surface position of the ITCZ (dashed line) and stretching westward from the Red Sea Hills to the central Sahel/Sahara (Fig. 6c). Corresponding low sea level pressure predominated over approximately the same regions. Nocturnal cooling in the region (Fig. 6d) was accompanied by persisting low pressure over the Red Sea and the Arabian Peninsula through 0300 LST, while high pressure expanded northward from the highland regions south of the gap (not shown), passing the TG entrance, triggering the jet, and eventually nearing the ITCZ. This chain of events marked the arrival of the monsoons at the ITCZ boundary, resulting in significant increased horizontal convergence in the lower-atmospheric winds.

c. *Ties to other orographic flows*

Timing of the increased surface pressure and convergence in the horizontal winds upstream of the gap

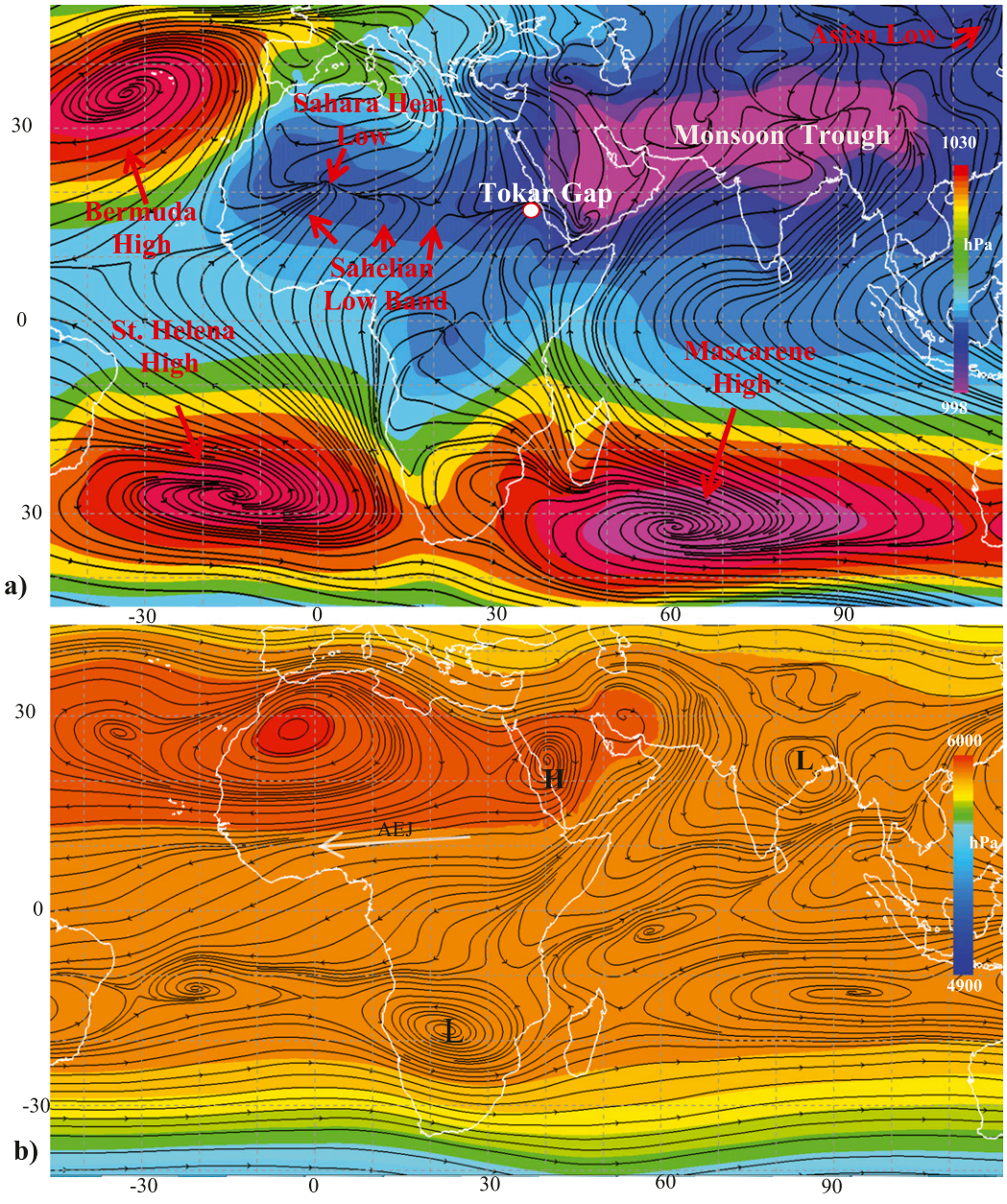

FIG. 3. (a) Sea level pressure (hPa; color contours) and 10-m streamlines for the period 10–20 July 2008 based on the NASA MERRA reanalysis. Major semipermanent pressure features and the location of the Tokar Gap are labeled in red. (b) Corresponding 500-hPa geopotential heights (m) and wind streamlines with high and low regions indicative of an active monsoon period labeled in black.

was directly linked to the progress of the monsoons as they were channeled around and through the topographic elements south of the TG. Among the key topographic features controlling the monsoon pathway(s) are the Red Sea Hills, the East African highlands (EAH), the Ethiopian highlands (EH), and the Turkana valley, sometimes referred to as the Lake Turkana valley (Fig. 1). Both the WRF Model and HYSPLIT simulations indicated that these features channel the southerly summer monsoons inland from 20°S to 20°N and toward the ITCZ and the TG. Some previous studies have discussed how regional orographic flows are central to the moisture transport to the EH (Viste and Sorteberg 2013a) as well as farther downwind across the Indian Ocean (Slingo et al. 2005). Other works have established that the orographic uplift experienced by the monsoons in this channeling process frequently leads to the development of well-organized mesoscale storms (Hill and

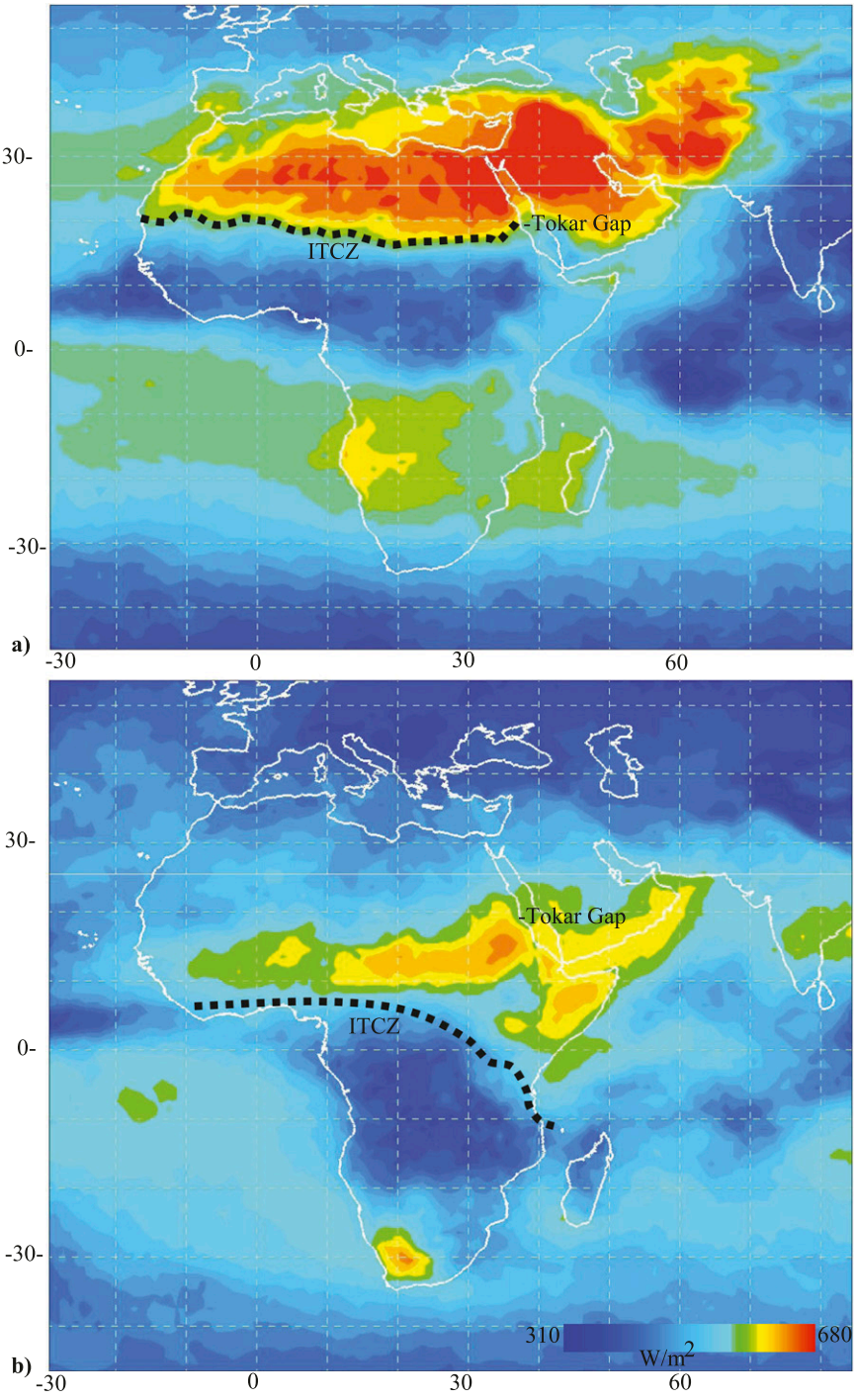

FIG. 4. AIRS total outgoing longwave radiation (OLR) for (a) July 2008 and (b) December 2007. Black dotted lines show the position of the surface ITCZ across the African continent at each time.

Lin 2003; Zhang et al. 2011). However, relatively little has been done to better understand how these particular regional flows may be connected to one other. We now explore the links between Turkana jet, the monsoon winds in the Turkana valley, and the gap flows in the Red Sea Hills.

As described by Kinuthia and Asnani (1982) the Turkana jet is a permanent low-level jet that passes

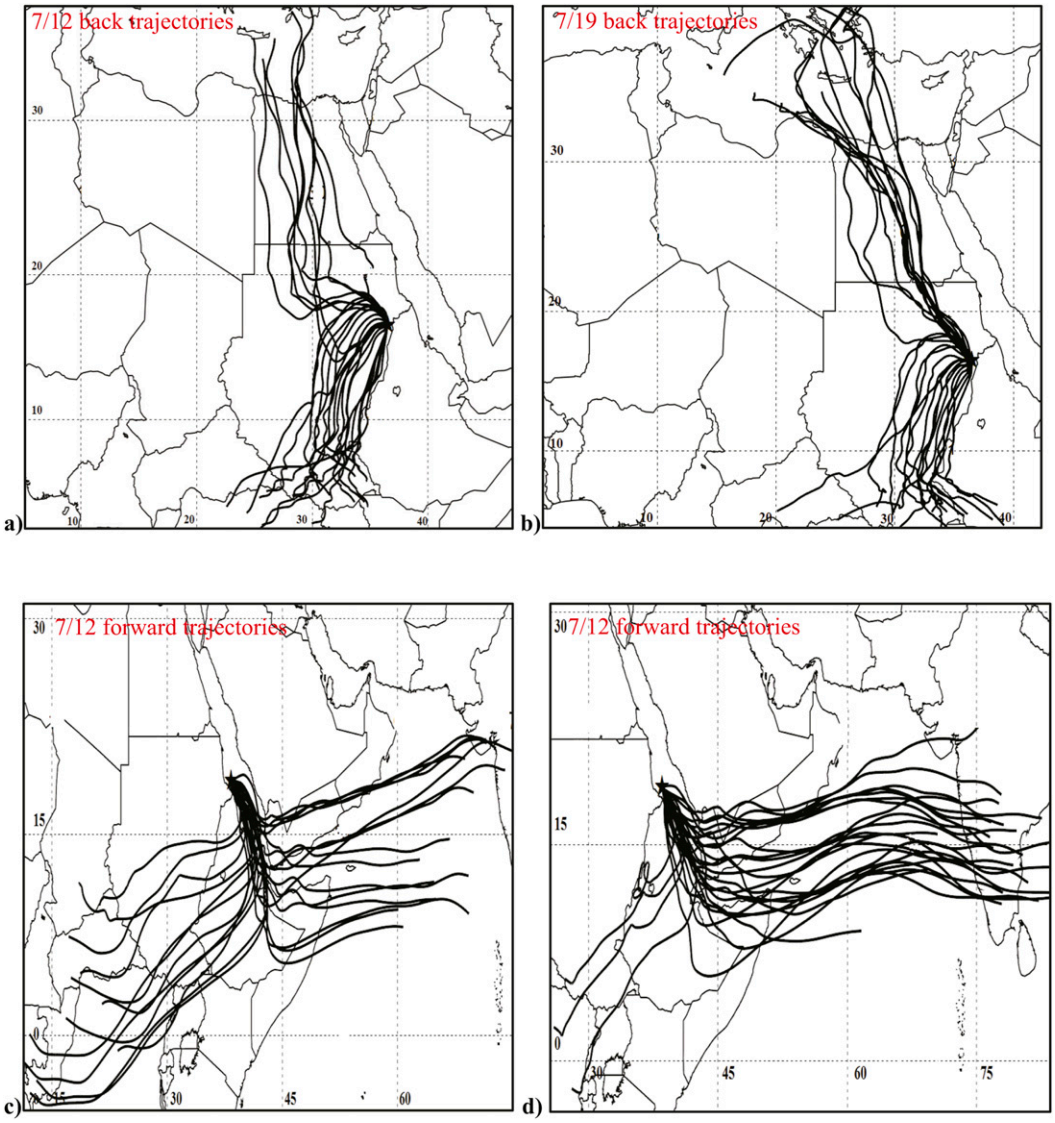

FIG. 5. HYSPLIT Lagrangian trajectories computed for TGJ events on 12 and 19 Jul 2008. (a),(b) Six-day back trajectories originating at the TG entrance during these events. (c),(d) Corresponding 6-day forward trajectories computed from the TG exit region.

through the Turkana valley formed between the EH and EAH (Fig. 1). This jet is essential to the advection of Indian Ocean moisture inland and to the accumulation of moisture in the EH/EAH region (Viste and Sorteberg 2013b; Sun et al. 1999). The jet flows northwestward and emerges from the Turkana valley near point B in Fig. 1. The movement of moist air northward from this point, and toward the Red Sea Hills, is shown in vertical sections of potential temperature and water vapor mixing ratio along the line AB pathway (Figs. 7a,b), taken at 0100 LST. Here the monsoon incursion resembles a cool, moist gravity current. Its leading edge, or ''monsoon front,'' has sharp meridional gradients in temperature and moisture. The front advances and retreats diurnally and its northward movement was at an approximate rate of $7\,\mathrm{m\,s^{-1}}$ at the time shown in Figs. 7a and 7b. This compares with an estimated range of $11–16\,\mathrm{m\,s^{-1}}$ for a 1.5-layer gravity current with speed $c \approx \alpha\sqrt{g'H}$, where $1 < \alpha < 1.3$, g' is the reduced gravity of roughly $0.16\,\mathrm{m\,s^{-2}}$, and $800\,\mathrm{m} < H < 1000\,\mathrm{m}$ is the height of the intrusion near the leading edge of the front. Throughout the cycle, the monsoons confined below 2000 m in altitude remained inclined as it undercut the Harmattan and/or Etesian airmasses near the ITCZ.

These same frontal characteristics distinguished the monsoon passage around the western Sahel/Sahara

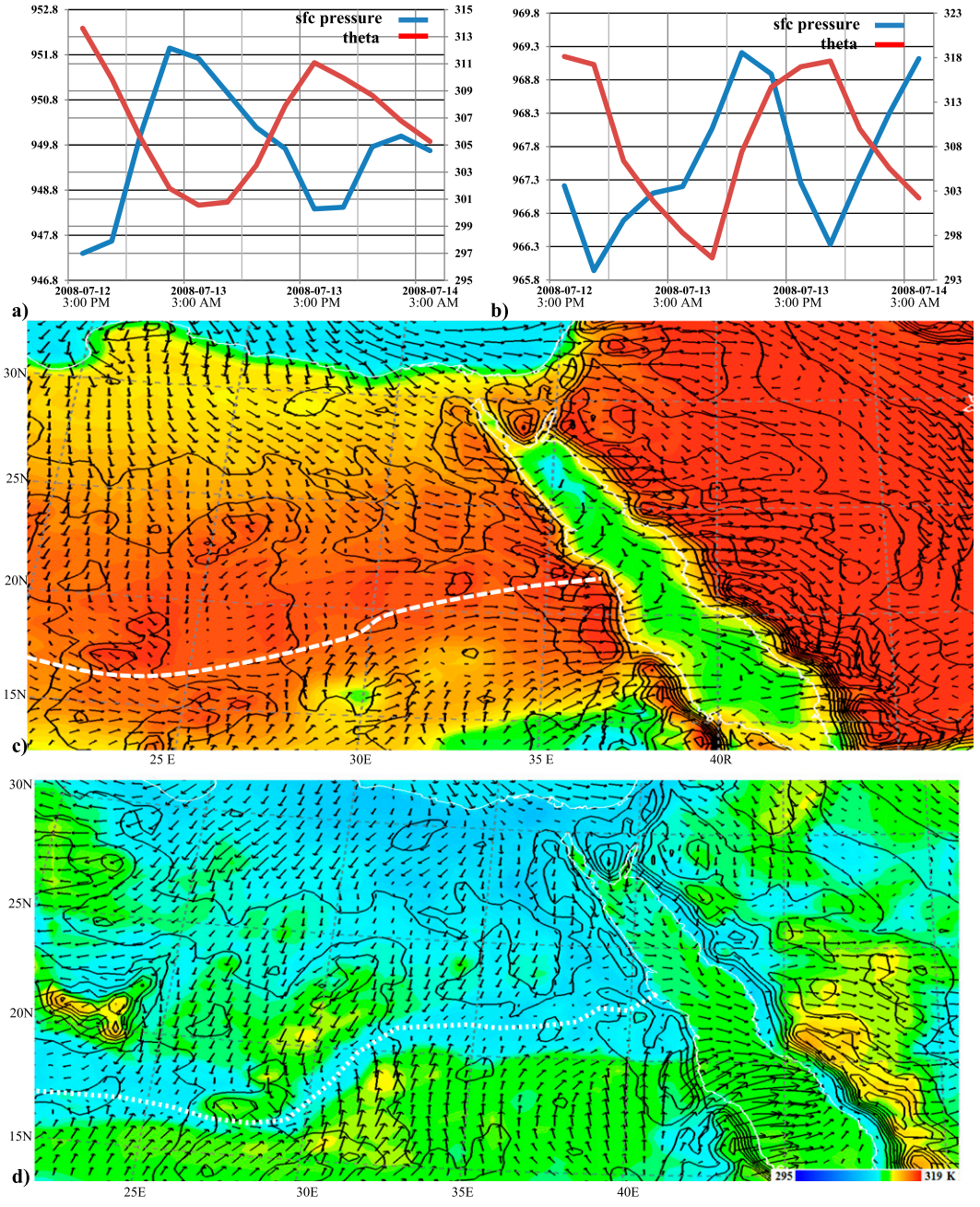

FIG. 6. The diurnal cycle of temperature and pressure over the ITCZ region in the eastern Sahel. Shown are time series of potential temperature and pressure over (a) the ITCZ and (b) the TGJ entrance. Also shown are snapshots of the WRF Model 10-m winds over line contours of topography and shaded color contours of 2-m potential temperature for (c) 1500 12 July and (d) 0300 13 July.

adjoining the Red Sea Hills. As in the vertical cross sections, this incursion over the model domain surface was discernable as a front of cooler, moist air moving northward from the base of the Turkana valley region (point B, Fig. 1) in response to the developing low pressure region just south of the ITCZ. Increased wind speed also accompanied the monsoon front, resulting in increased convergence in the horizontal winds as it approached the latitude of the TG and surface ITCZ. A key finding based on the WRF Model simulations was that the onset of the TGJ, as well as the gap winds through the secondary gaps to the north and south of the TG, coincided with monsoon front arrival and passage. This essential role of the monsoon front in the forcing of the TGJ and

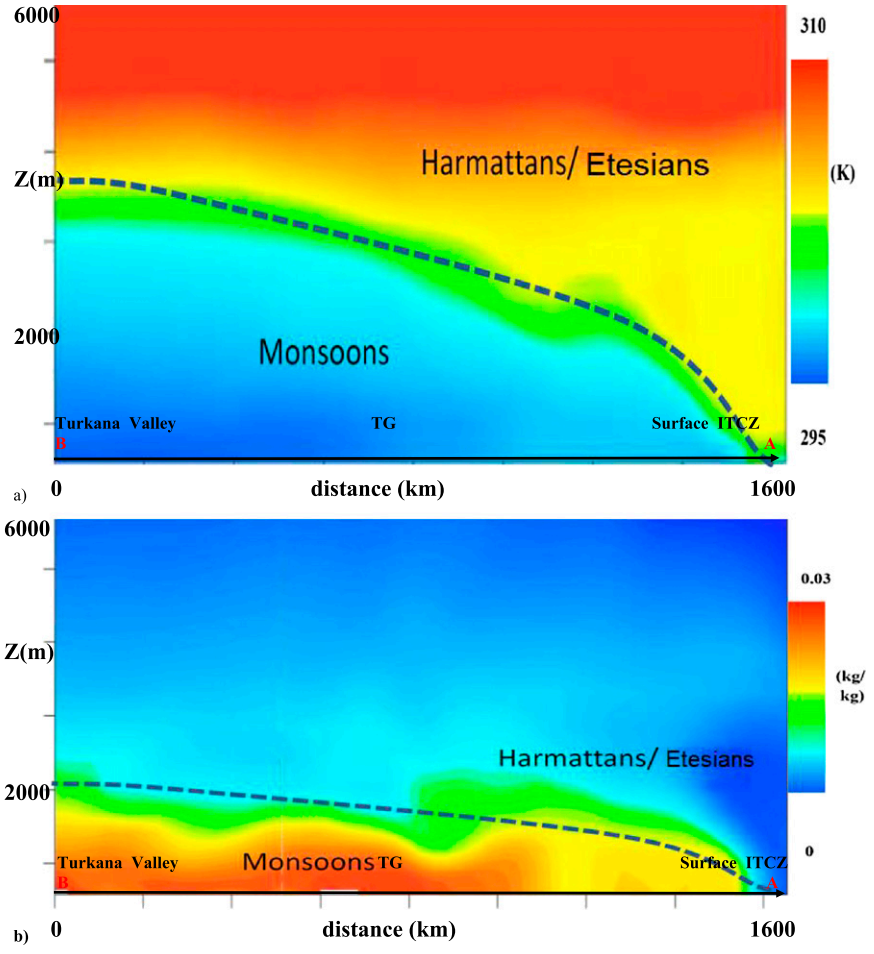

FIG. 7. The monsoon inflow on 12 Jul 2008 are seen through cross sections of (a) potential temperature and (b) the water vapor mixing ratio along the AB line connecting the Turkana valley and the ITCZ at 0100. The leading edge of the monsoon front is indicated by the blue dashed lines.

secondary gap winds emanating from the Red Sea Hills will be illustrated further in the case studies in section 5.

d. Upstream influences: The land–sea breeze cycle

The local land–sea breeze cycle plays a significant role in the TGJ's behavior and is a persistent mesoscale feature in the coastal Red Sea region. Early documentation of the regional sea breeze noted its regularity (Pedgley 1974; Steedman and Ashour 1976), especially in summer months. Like the TGJ, the regional sea breeze is characterized by strong diurnal variability between the months of June and August. Further striking features observed by these authors were the large inland reach of the sea-breeze front and the cycle's close relationship with the onset and relaxation of the TGJ.

Pedgley (1974) observed that a sea-breeze front develops during the morning some 10–20 km inland and advances away from the coast, sometimes reaching 100 km offshore by evening. The sources and coverage of Pedgley's data along the Sudan coast are not clear. The ensuing work by Steedman and Ashour (1976) found that in the northern and central Red Sea regions, sea-breeze impacts could be measured as far as 225 km inland over the Arabian Peninsula with wind intensities reaching an average of 6.7 m s^{-1}. However no observations along the African Red Sea coast were presented in that study. In the summer 2008 WRF Model simulations, the sea breeze reached inland ~130 km within and around the Tokar Gap in most cases (e.g., Figs. 8a–c) and occasionally incurred in excess of 200 km. WRF Model sea-breeze incursions elsewhere along the Red Sea Hills were limited to 10–20 km. Wind speeds observed in the simulated sea breezes ranged from 3 to 10 m s^{-1} and were comparable in magnitude to observations along the Arabian coast by Steedman and Ashour (1976) and Pedgley (1974).

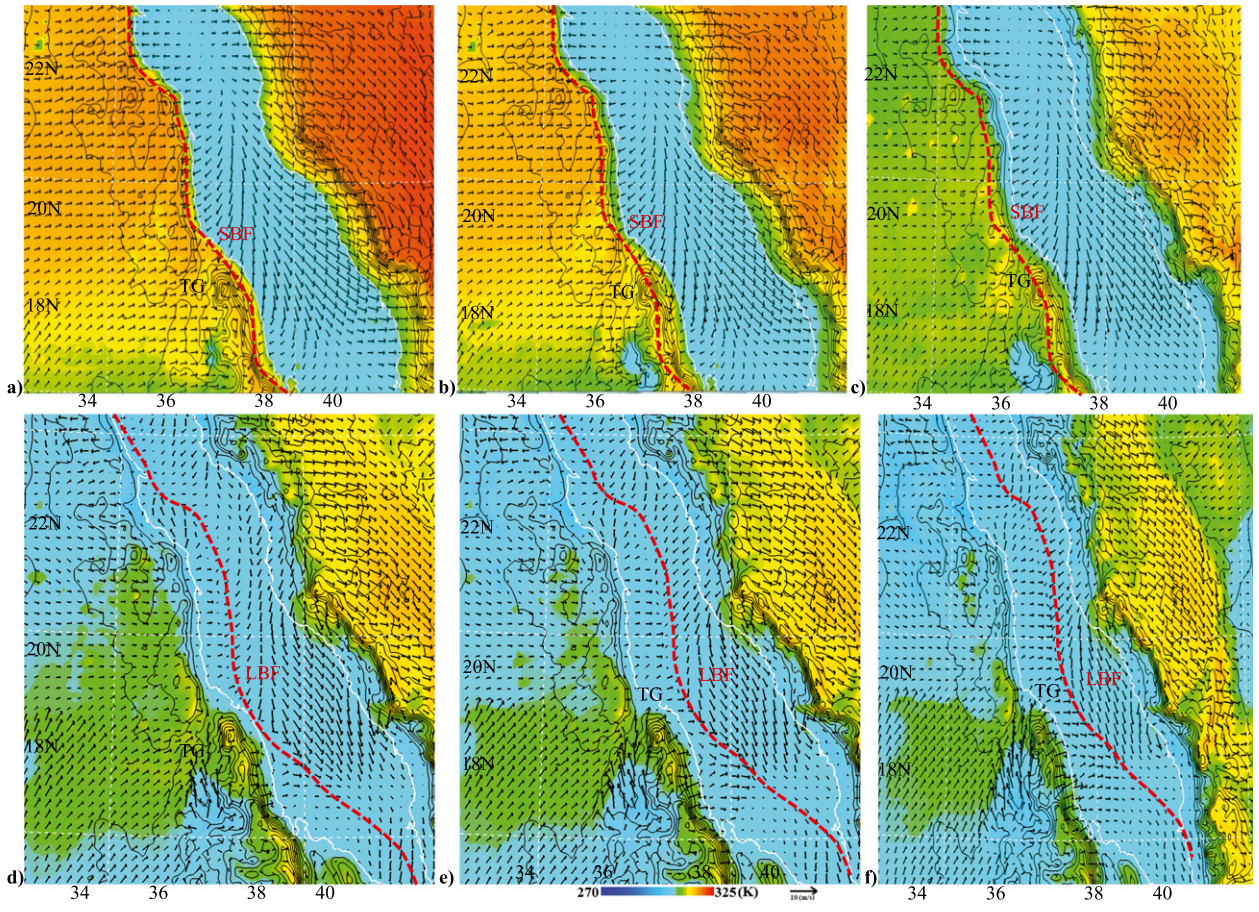

FIG. 8. WRF Model simulations of the Red Sea sea breeze and land breeze on the day prior to the extreme jet study, 11 Jul 2008. Shown are 10-m winds and color contours of 2-m potential temperature over black contours of topography at (a) 1700, (b) 1800 (c) 1900, (d) 2100, (e) 2200, and (f) 2300 LST. Dashed lines denote the position of the sea breeze and land breeze fronts.

The cycles of the land–sea breeze and the TGJ share common roots in the extreme diurnal heating pattern occurring in the regional continental atmosphere. In comparison with the Steedman and Ashour (1976) and Pedgley (1974) observations on the eastern coast of the Red Sea, the WRF Model simulations indicated sea-breeze development at the west coast somewhat later in the day, with formation of the sea-breeze front (SBF) occurring around 1500 LST and with inland flow maintained throughout the afternoon (Figs. 8a,b). In addition, the WRF Model sea breeze front forms within a fetch range 10–30 km inland along the coastal plain extending from the Red Sea Hills. Simulations rendered steady inland flow following the onset of the sea breeze with the inland incursion typically reaching its peak in early evening (Fig. 8c).

The land-breeze phase of the cycle also developed over 3–5 h spans in the WRF Model simulations and often was more difficult to detect in the simulations because of its closeness in timing with the onset of the TGJ. As seen in Figs. 8d–f, the land breeze developed as basinwide offshore flow formed around 2100 LST (Fig. 8d). A land-breeze front is clearly evident in the 10-m wind field at this time at 50–60-km fetch offshore from the Tokar delta and moving progressively further from shore between 2100 and 2200 LST (Fig. 8e). It is important to note that there is no significant outflow from the Tokar Gap at this stage, suggesting that it is the monsoon front, and not the land breeze, that triggers the outflow. At 2300 LST (Fig. 8f), the arrival of the monsoons from the south can be seen at the entrance of the Tokar Gap along with the early stages of the TGJ development.

5. Case studies

The aforementioned elements of the TGJ and its forcing mechanisms can be described in the context of two case studies. Both events examined here were present in the model simulations during July 2008, which can be considered an ‘‘active monsoon period’’ as described

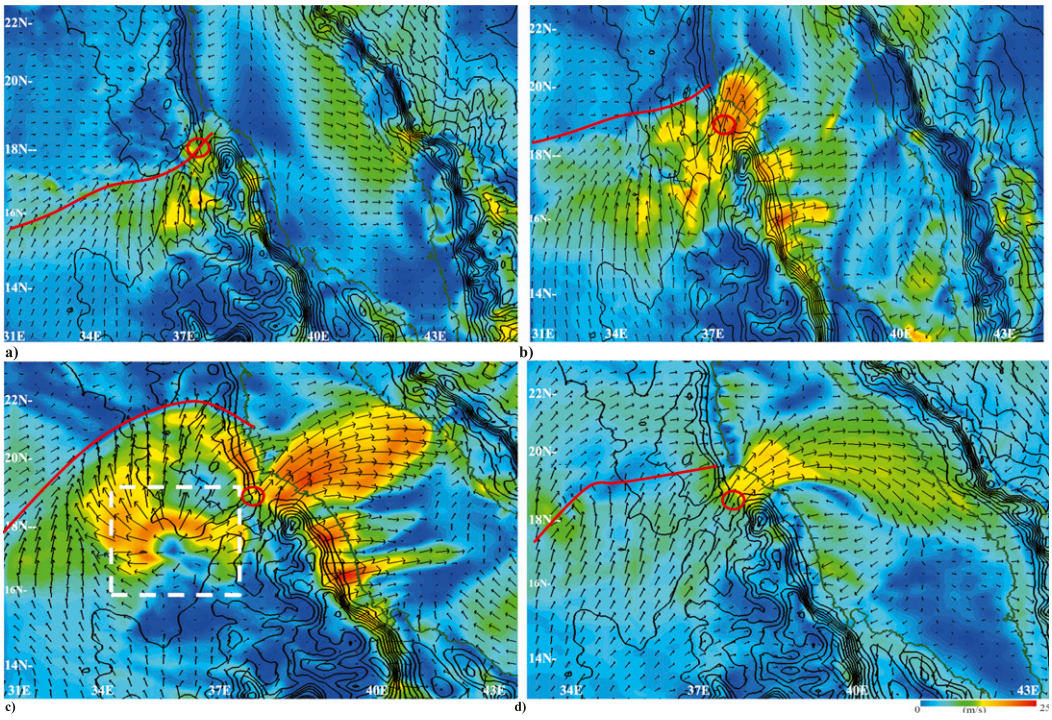

FIG. 9. WRF Model–simulated conditions for the 12 July TGJ event. Shown are 10-m wind vectors with color contours of wind speed ($m\,s^{-1}$) and line contours of topography (250 m interval) at (a) 1900 (12 July), (b) 2200 (12 July), (c) 0300 (13 July), and (d) 1300 LST (13 July). Red lines indicate the leading edge of the monsoon front and red circles indicate the location coinciding with the Hovmöller diagrams shown in Fig. 10. A white box in (c) indicates the location of the MCC downburst identified in the simulation of conditions that day.

by Ramaswamy (1962) with a trough in the 500-hPa heights extending eastward from the Indian subcontinent to East Africa and an anticyclone situated over the Arabian Peninsula (Fig. 3b) . However, as pointed out in Jiang et al. (2009), TGJ activity occurred on a near daily basis throughout the summer months of 2008 and 2009, suggesting the active and break periods of the monsoons modulated the TGJ intensity but not its diurnal periodicity. With this, we first look to an extreme event that occurred on 12–13 July with winds exiting the Tokar delta exceeding $25\,m\,s^{-1}$. The second case study centers on conditions on 19–20 July and is representative of TGJ flows between 1 June and 31 August 2008 that are stronger than average but not extreme.

a. An extreme jet event

Conditions on 12 and 13 July 2008 contributed to one of the most intense TGJ events observed that summer. At 1900 LST, as seen in Fig. 9a, the sea breeze and prevailing onshore flow were present along the Red Sea Hills north of the TG while the arrival of the monsoon front and the remnants of the land breeze were observed around the TG and secondary gaps to the south. Figure 9b presents conditions 3 h later with development of a jet flow clearly evident in the TG and secondary gaps while the monsoons continued their northward advance. At 0300 LST 13 July, the TGJ reached maximum intensity with sustained winds of $26\,m\,s^{-1}$ while extending across the full width of the basin (Fig. 9c). At this time a downburst indicative of a developing mesoscale convective complex appeared at the northern rim of the TG entrance, a feature discussed further below. With the monsoon front retreating south from the surface ITCZ, the TGJ began to relax at 1300 LST (Fig. 9d) This coincided with the development of a pronounced anticyclonic jet curvature (~160 km in the model) over the Red Sea, a value comparable to an inertial radius of $U/f \sim 119$ km, where U is the mean jet wind speed, with a mean value of about $16\,m\,s^{-1}$ and $f = 1.34 \times 10^{-4}\,s^{-1}$. The curvature was so pronounced as to produce a strong westward return flow toward the Red Sea Hills and African highlands.

The evolution of the vertical structure of the TGJ during the extreme event is seen in the Hovmöller diagrams (Fig. 10) of selected jet properties measured at a point located in the exit region (the Tokar delta). The location of the plot is indicated by a red circle in Fig. 9. Figure 10a shows that the model-simulated gap jet reached sustained wind speeds of $26\,m\,s^{-1}$ in the jet core,

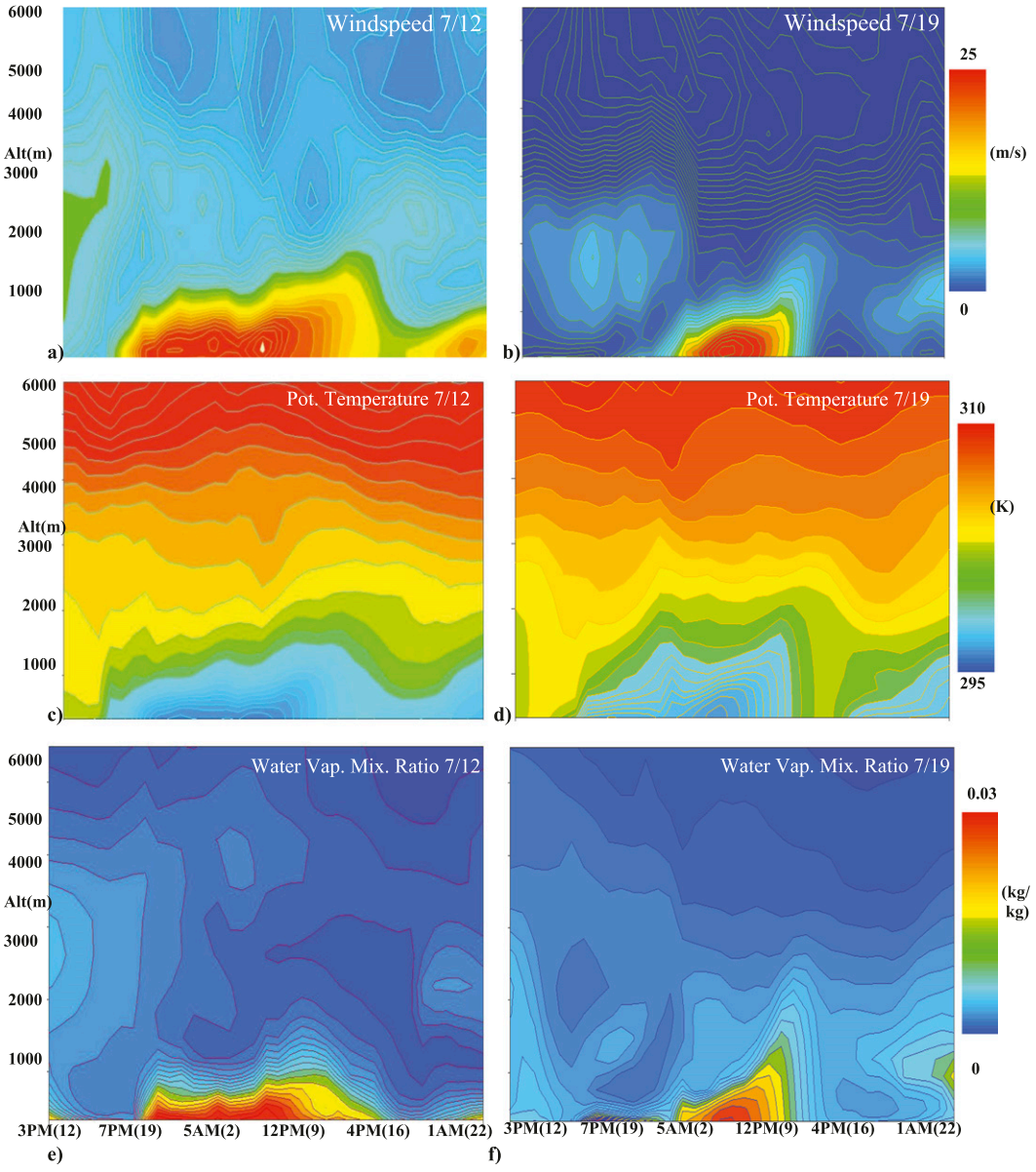

FIG. 10. Hovmöller diagrams of jet properties at the TGJ exit region/TG delta. Shown are diagrams of the evolution of wind speed during the (a) 12 July and (b) 19 July case studies, and corresponding diagrams of (c),(d) potential temperature and (e),(f) water vapor mixing ratio. Times shown are in LST with UTC counterparts in parentheses.

which extends up to 600–800 m in altitude. Sharp gradients in wind speed confirm that the onset of the TGJ on 12 July occurred around 1900 LST and maintained its jet properties until 1600 of the next day (13 July). The model simulations further show the vertical extent of the jet reaching near 1600-m altitude during the later stages. The core of the jet initially developed at ground level but elevated to around 700 m in altitude toward the end of the event. Further evidence of the monsoon forcing was seen in the cool, moist nature of the Hovmöller profiles of potential temperature and water vapor mixing ratio at the TG exit. Figure 10c shows that the vertical and temporal evolution of the potential temperature in the TGJ time frame mirrored that seen in wind speed. In terms of moisture, it was seen (Fig. 10e) that the 12 July TGJ event was marked by significant elevations in the water vapor mixing ratio in a 300–700-m-thick layer just above the surface. This enhancement persisted throughout the event with sharp temporal gradients coinciding with the jet onset and following its passage.

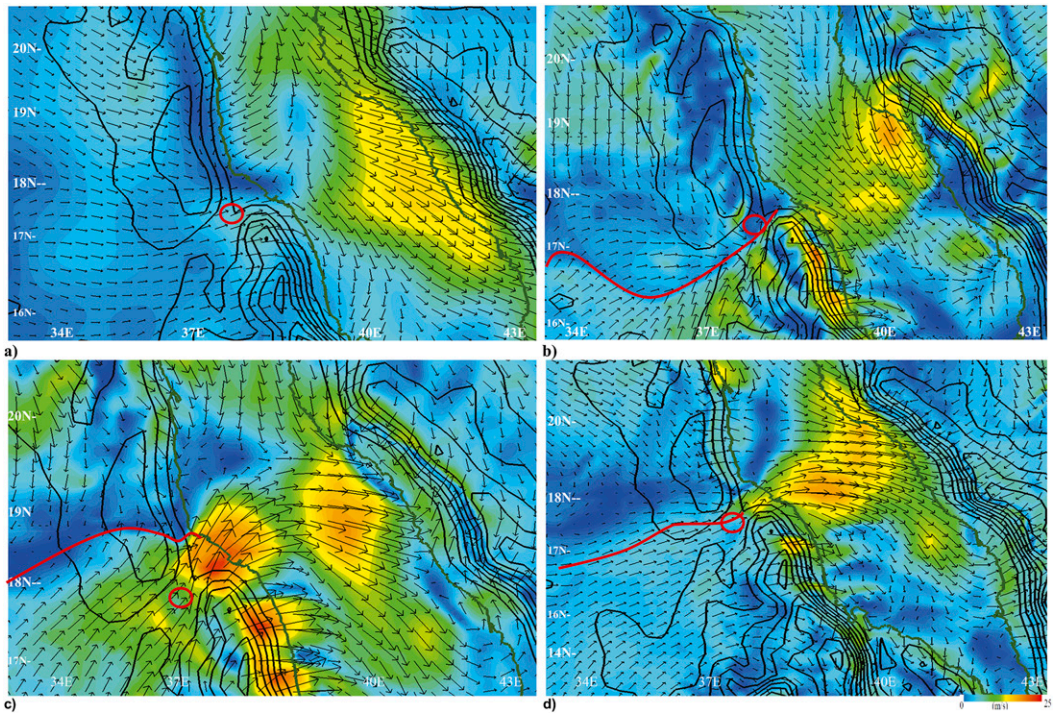

FIG. 11. WRF Model–simulated conditions for the 19 July TGJ event. Shown are 10-m wind vectors with color contours of wind speed ($m\,s^{-1}$) and line contours of topography (250 m interval) at (a) 1500 (19 July), (b) 0100 (20 July), (c) 0900 (20 July), and (d) 1300 LST (20 July). Red lines indicate the leading edge of the monsoon front and red circles are the locations coinciding with the Hovmöller diagrams shown in Fig. 10.

b. A typical strong TGJ summer event

According to the WRF Model record of jet events during July–August 2008, as shown in Fig. 2 of Jiang et al. (2009), the 12–13 July event was the strongest observed that season. There are also approximately 16 other events out of a total of 43 that are stronger than average in terms of the area percentage over which winds exceeded $10\,m\,s^{-1}$. We now examine a typical example of these stronger events: one that occurred on 19 July.

Typical TGJ events observed during the July and August time frame were weaker in terms of maximum sustained wind speed yet retained strong structural similarities to those seen in the 12 July extreme event. It appeared that these more typical events were driven by weaker monsoon forcing from the south (just north of the Turkana valley exit region), where the monsoon winds sustained speeds between 4 and $6\,m\,s^{-1}$ for a 25-h period during the 19 July jet event versus 8–$10\,m\,s^{-1}$ for 37 h for the more extreme 12 July case. With this, the more typical jets were modulated to a greater extent by the regional sea-breeze cycle. This was readily discernible in the model conditions at 1500 LST 19 July as shown in Fig. 11a. At this time, the full development of the regional afternoon sea breeze prevailed across the east and west coastlines of the Red Sea. Onshore flow in the vicinity of the TG was associated with the local sea breeze and possibly enhanced by strong northwesterly flow along the Red Sea axis that persisted for 10 h. There was also a much longer transition period (6-h difference) from the sea-breeze to land-breeze phase of the cycle than seen one week prior. It is not until 10 h later, at 0100 LST 20 July, that the arrival of the monsoon front is detected in the 10-m winds (Fig. 11b). The arrival of the monsoon front coincides with the initial stages of the gap jet formation in the TG and secondary gaps. In the 0900 LST snapshot seen in Fig. 11c, the full development of the TGJ across the basin can be seen while the monsoon front has progressed only slightly north of the TG. By 1300 on the following day (Fig. 11d) the TGJ is still present, though weaker, and the secondary jets have nearly disappeared. A comparison of Figs. 9d and 11d suggests that the return flow from the Red Sea to the EAH is much less pronounced in the 19–20 July event.

In the examination of the vertical profiles presented in Figs. 10b, 10d, and 10f, it is seen that the model-simulated vertical structure of the 19 July TGJ maintained strong similarities to those in the extreme jet case. The Hovmöller diagram of model wind speed at the TG exit shown in Fig. 10b indicates that onset of the 19 July jet

occurred near 0400 LST. This onset was 5 h later than that observed during the 12 July case study. The duration of the 19 July jet was shorter as well, lasting a little more than 8 h versus the 14+ h sustained in the 12 July extreme jet case. Maximum wind speeds were ~22 m s^{-1} and occurred between the surface and 500 m in altitude. As was the case with the 12–13 July event, vertical penetration of the 19 July jet increased with time, with disturbances in velocity, water vapor content, and potential temperature reaching 2000 m or more in altitude near the end of the event (Figs. 10b, d,f). The strongest signal remained below about 850 m, which is slightly shallower than the 1000–1200-m height of the 12 July extreme case. Yet despite differences in timing and duration, the unique cool, moist core of the jet induced by the nocturnal monsoon forcing was readily distinguishable in the evolution of the 19 July jet. This signature as observed in both case studies is an extraordinary feature of TGJ in comparison to other notable gap winds such as the Central American Tehuantepec gap winds and Papagayo gap winds, which tend to be warm and dry (Magaña et al. 1999; Sun and Yu 2006; Romero-Centeno et al. 2007; Karnauskas et al. 2013). This unique characteristic also features prominently in the impacts of the TGJ downwind.

6. Moisture transport

a. Regional moisture transport

Understanding the variability in the orographic flow and moisture transport within eastern Africa is central to the region's rainfall patterns (Slingo et al. 2005). For the EH/EAH and eastern Sahel, a rainy season occurs during the months of June–September, coinciding with the northward movement of the ITCZ and the peak inflow from the monsoon winds. Rainfall during these months accounts for 50%–90% of the annual precipitation (Griffiths 1972; Viste and Sorteberg 2013a) with the range dependent upon the moisture transport achieved. Recent interests have additionally focused upon regional moisture transport, its bearing upon Sahelian rainfall, and its influence upon tropical cyclogenesis achieved over the Atlantic Ocean basin. Such studies center upon the role of the East African and Ethiopian highlands as a center of moisture collection and redistribution through mesoscale storm rainfall. However, the role of moisture transport by the East African orographic flows, including the Tokar and Turkana jets, is unexplored. For the 8-day period spanning the 12 and 19 July events, WRF Model simulations suggest that the TGJ can play a significant role in moisture budgets within the EARSAP region and can cause strong elevations in surface latent heat fluxes over the Red Sea.

b. Latent heat fluxes

In these WRF Model simulations, 2-m latent heat fluxes are determined via the YSU boundary layer scheme used and calculated following the method of Carlson and Boland (1978). This implies that

$$q^* = -\overline{q'w'}/u^*,$$

where q^* is the latent heat flux, q' and w' are the perturbations of moisture and vertical velocity respectively, and u^* is the friction velocity defined by

$$u^{*2} = \overline{u'w'}^2 + \overline{v'w'}^2 = \tau/\rho.$$

Here u' and v' are the perturbations in horizontal velocity, and w' is the perturbation in vertical velocity. The frictional velocity can also be viewed as the ratio of the surface stress, over the density ρ of the lowermost layer in the model. The WRF Model simulations indicated that the TGJ and secondary gap flows drove extreme elevations in the latent fluxes over a significant portion of the central/southern Red Sea during the 12 July event as seen in the peak model latent heat flux for the event shown in Fig. 12a. As the time series shows in Fig. 12b, this elevation in flux intensity paralleled the development of the gap jet itself, with the rise in latent heat flux at the TGJ exit rising from 12 W m^{-2} prior to the jet development at 2200 LST to a maximum of 903 W m^{-2} at 0600 LST as the TGJ reached its peak intensity (Fig. 12b). Remarkably, latent heat fluxes just offshore of the gap are sustained above 300 W m^{-2} for a 24-h period. Putting this in context, typical latent heat fluxes in the Gulf Stream region throughout summertime are in the 200–300 W m^{-2} range (Talley et al. 2011) while observed values in Atlantic tropical cyclones have ranged from maximums of 600 W m^{-2} in Hurricane Alberto to 1400 W m^{-2} in Hurricane Isabel (Liu et al. 2011). The magnitude and location of these enhanced fluxes directly influence the downwind evolution of the lower atmospheric water vapor mixing ratio (Fig. 12c) and in turn could have a bearing on the regional rainfall patterns in the manner established by Viste and Sorteberg (2013a).

As the Lagrangian forward trajectories (Figs. 5c,d) suggest, a significant portion of the downwind TGJ transport during the 12 July event may enter to the African highlands. The return circulation set up by the anticyclonic veering of the jet (Fig. 9d) is responsible for at least some of this inland flow. The inshore flow is clearly observed to the south of the TG, especially within the secondary gaps to the south, the Afar basin, and the base of the EH. This wide swath of influence of the jet and its

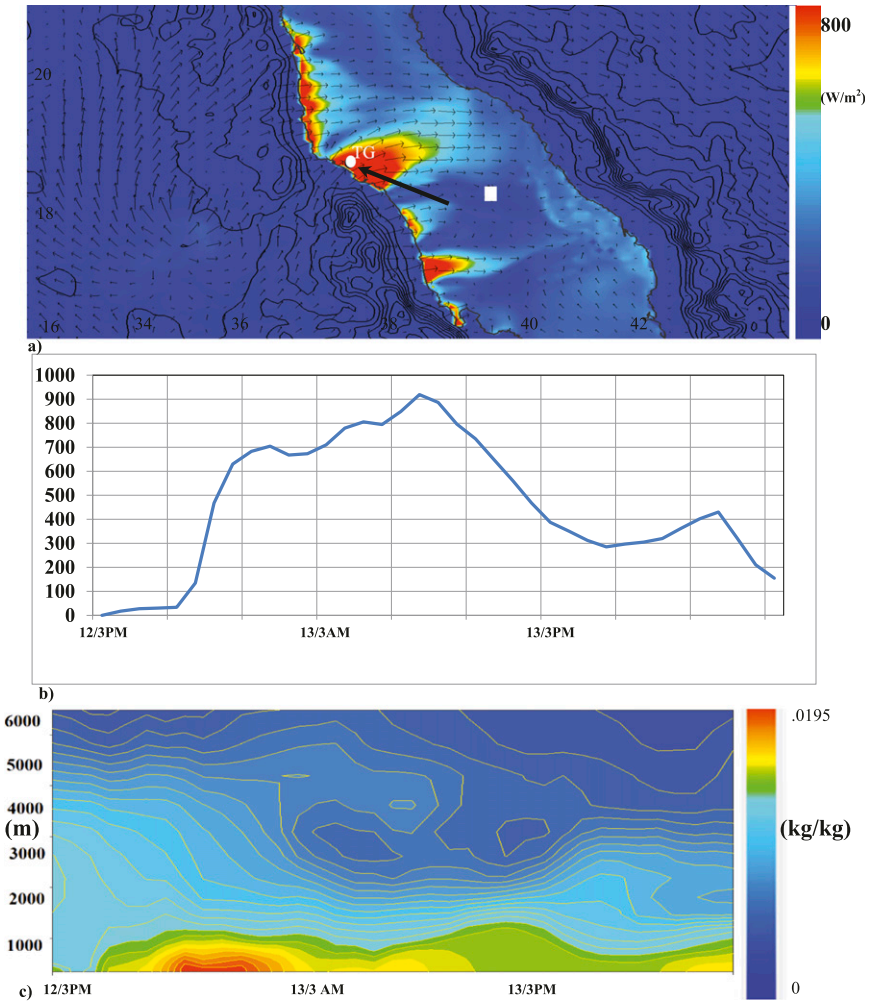

FIG. 12. WRF Model–simulated latent heat fluxes (LHFs) at 0600 13 July. (a) Color contours of LHFs (W m^{-2}) from the TGJ and secondary gaps with 10-m wind vectors and (b) the time series evolution of the LHF at the TGJ exit [black arrow in (a)] during this event. (c) A Hovmöller diagram shows the time/height characteristics of the water vapor mixing ratio over the Red Sea downwind of the Tokar Gap (white square).

curvature and recirculation parallel characteristics observed in simulations of the Tehuantepec gap jet (Steenburgh et al. 1998). An estimate of the magnitude of moisture transported is presented next.

c. *Horizontal moisture transport*

To quantitatively evaluate the moisture flux achieved by TGJ and neighboring gap jet flows, integrated moisture fluxes were calculated over the 8-day time frame spanning the two TGJ case studies. Specifically, attention was given to the WRF Model–derived fluxes across the boundaries of two subregions of interest within the high-resolution domain. Figure 13a presents the location and configuration of the subregions used in this portion of our analysis. The first box encloses the central Red Sea, a principal route of regional transport established in studies by Viste and Sorteberg (2013a). The second envelops the Ethiopian highlands, which numerous previous studies (e.g., Viste and Sorteberg 2013a; Hill and Lin 2003) have established as the critical center for collecting atmospheric moisture and redistributing it throughout the region via convective rain storms and numerous rivers (including the Blue Nile) whose headwaters are situated in this mountainous region.

Thus we turn to an estimation of the TGJ and secondary gap wind contribution to the moisture transport based on the construction of a water vapor budget in the highlands and Red Sea regions. At any position along a box boundary, the vertically integrated moisture mass flux was calculated as

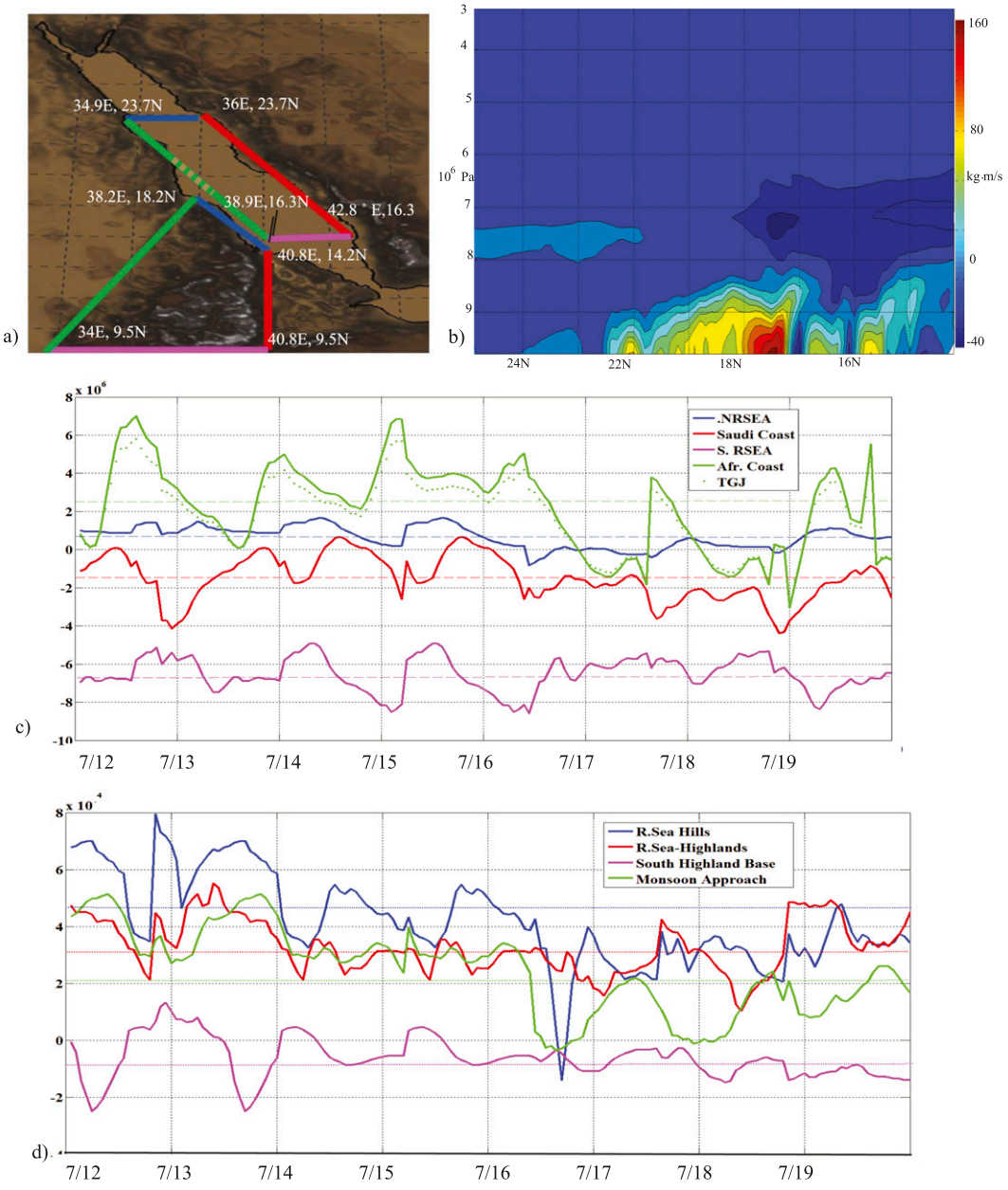

FIG. 13. Subregions of interest with respect to the EARSAP moisture transport and IMFs from the WRF Model simulation. (a) The configuration of the subregions over the Red Sea and around the African highlands and (b) a vertical profile of the fluxes along the Red Sea coast/TGJ side. The simulated IMFs ($\mathrm{kg\,s^{-1}}$) between 12 and 19 Jul 2008 for (c) each side of the African highland subregion and (d) the Red Sea subregion.

$$\text{flux} = \frac{1}{g}\int_{\text{sfc}}^{8000\text{Pa}} v_n q\, dp,$$

where q is the model specific humidity, v_n is the model incident velocity normal to the face of the boundary, 8000 Pa (80 mb) represents the top of the model domain, and dp is the vertical incremental change in pressure. Units of this flux are in $\mathrm{kg\,m^{-1}\,s^{-1}}$. In the analysis shown here, the integrated moisture flux (IMF) along a boundary ($\int \text{flux}\, dl$, with unit $\mathrm{kg\,s^{-1}}$) maintains the convention that positive (negative) values indicate transport of water vapor into (out of) the box.

The central Red Sea box (Fig. 13a) used in the moisture budget analysis was designed to evaluate contributions from the TGJ and secondary flows relative to those due to the winds blowing along the length of the Red Sea. Thus, two borders were established across the long axis of the Red Sea to capture the moisture influx

from the northern Red Sea (blue line) and the outflow to the southern Red Sea (magenta line). A border tangential to the western Red Sea coast (green line) was constructed to evaluate the influences of the TGJ and secondary flows while a border tangential to the western Red Sea coastline enabled an evaluation of the outflow to the Saudi Peninsula.

A representative vertical cross section of the moisture flux (q^*v_n) during the peak of the 12–13 July extreme event at 0300 along the Red Sea coast is presented in Fig. 13b. There, the large influx into the Red Sea box generated by the TGJ and secondary flows can be seen. The relative low-altitude nature of the influx is also evident in this figure, characterizing the model moisture fluxes into the Red Sea box as well as the highland box, during the period of interest.

As shown in Fig. 13c, a large influx of moisture into the Red Sea box was seen from the TGJ side (green curve). An estimate of the TGJ contribution alone is indicated by the dotted green curve, which corresponds to the dotted green section in Fig. 13a. The fluxes on the opposite side of the Red Sea (red curve) indicate net outflow and also exhibite strong diurnal variability, out of phase with flux variations on the west side.

Through cross-correlation analysis, a correlation coefficient of 0.79 between the TGJ influx and corresponding outflux on the Arabian side of the box, with a phase lag of 7 h observed between the signals, was obtained during the 1-week period. Because of lower specific humidity over the northern Red Sea, a relatively small net inflow of moisture was observed across the northern (blue) side of the Red Sea box due to the prevailing northwesterly winds over the northern Red Sea (RS).

The influx into the Red Sea from the TGJ and secondary flows reached 5.8 and $7.0 \times 10^6\,\mathrm{kg\,s^{-1}}$ respectively. Generally the subregion border along the Saudi coast recorded instances of significant moisture outflow ($\sim$2–4 $\times$ $10^6\,\mathrm{kg\,s^{-1}}$). The greatest loss from the subdomain was achieved along the southern Red Sea border and exceeded $8 \times 10^6\,\mathrm{kg\,s^{-1}}$ on three days. This large outflow is presumed to be tied to the large periodic inflow from the TGJ/east coast border acting in concert with the steady influx from the northern Red Sea region (i.e., atmospheric moisture delivered by TGJ/west coast combines with the already significant moist flow over the Red Sea). Mean IMF values during the week were of course lower but maintained similar trends, measuring $6.5 \times 10^5\,\mathrm{kg\,s^{-1}}$ across the northern Red Sea boundary, $-1.6 \times 10^6\,\mathrm{kg\,s^{-1}}$ across the Saudi/Red Sea border, $-6.5 \times 10^6\,\mathrm{kg\,s^{-1}}$ across the southern Red Sea boundary, and $2.2 \times 10^6\,\mathrm{kg\,s^{-1}}$ across the Tokar Gap/eastern Red Sea boundary. The implied net outflow of $5.25 \times 10^6\,\mathrm{kg\,s^{-1}}$ is equivalent to an annual evaporation rate of $0.46\,\mathrm{m\,yr^{-1}}$ over the surface area enclosed in this Red Sea box.

Model IMFs and the distribution of water vapor over the Red Sea in the model were consistent with Tomasi's (1984) observational survey, which found enhanced levels in the central and southern portions of the basin. As noted in the analysis by Chakraborty et al. (2006), precipitation events across the Red Sea were limited, despite the high level of water vapor mixing ratios, even in summer. In their findings the authors cited the absence of moisture flux convergence as a leading factor behind this limitation.

The highland box was constructed to examine the IMFs into a region of known elevated rainfall in the model simulations. As shown in Fig. 13a, a border was constructed to capture the influence of the TGJ return flow and moisture influx from the southern Red Sea directly into the elevated regions (blue line). An adjoining border (red line) was constructed to capture elements of the RS return flow through the Afar depression between the East African and Ethiopian highlands. Direct inflow and outflow along the southern extreme of the highland region were evaluated, as marked by a magenta line. The final (green) border for the highland box was established to gauge the IMF along the approach of the monsoons from the south/Turkana valley region to the TG as represented by the green line.

The evolution of the IMF in this highland subregion between 12 and 19 July is shown in Fig. 13d. Throughout this period, positive moisture influxes were recorded through the Red Sea Hills side (blue line), the Red Sea/highlands side (red line), and the western monsoon approach side (green line). In a general comparison, IMFs were smaller around the highlands than those observed over the Red Sea region. A net outflux of atmospheric moisture along the southern base of the highlands (magenta line) persisted throughout most of the same time period. The maximum influx was observed along the Red Sea Hills side of the region and reached $1.65 \times 10^5\,\mathrm{kg\,s^{-1}}$ following the 12–13 July extreme TGJ event. Indeed, timing of IMF maxima along this side of the box corresponded closely with the TGJ events observed that week, with a similar quasi-diurnal behavior. A corresponding maximum outflux was observed across the south highland (magenta) border following the extreme jet event as well with peak outflow throughout the week occurring 180 degrees out of phase with the peak influx periods (blue curve) along the Red Sea coast. Mean IMF values for the week study were $4.2 \times 10^4\,\mathrm{kg\,s^{-1}}$ along the Red Sea coast, $3.3 \times 10^4\,\mathrm{kg\,s^{-1}}$ from the Red Sea to the base of the EH, $-6.2 \times 10^3\,\mathrm{kg\,s^{-1}}$ along the base of the EAH/EH, and $2.9 \times 10^4\,\mathrm{kg\,s^{-1}}$ along the approach to the TG adjacent to the highlands. Thus there is a net influx of $4.2 \times 10^4\,\mathrm{kg\,s^{-1}}$ into the highland box during the period of study.

Orographic lifting over the East African topography contributed to development of clouds and mesoscale

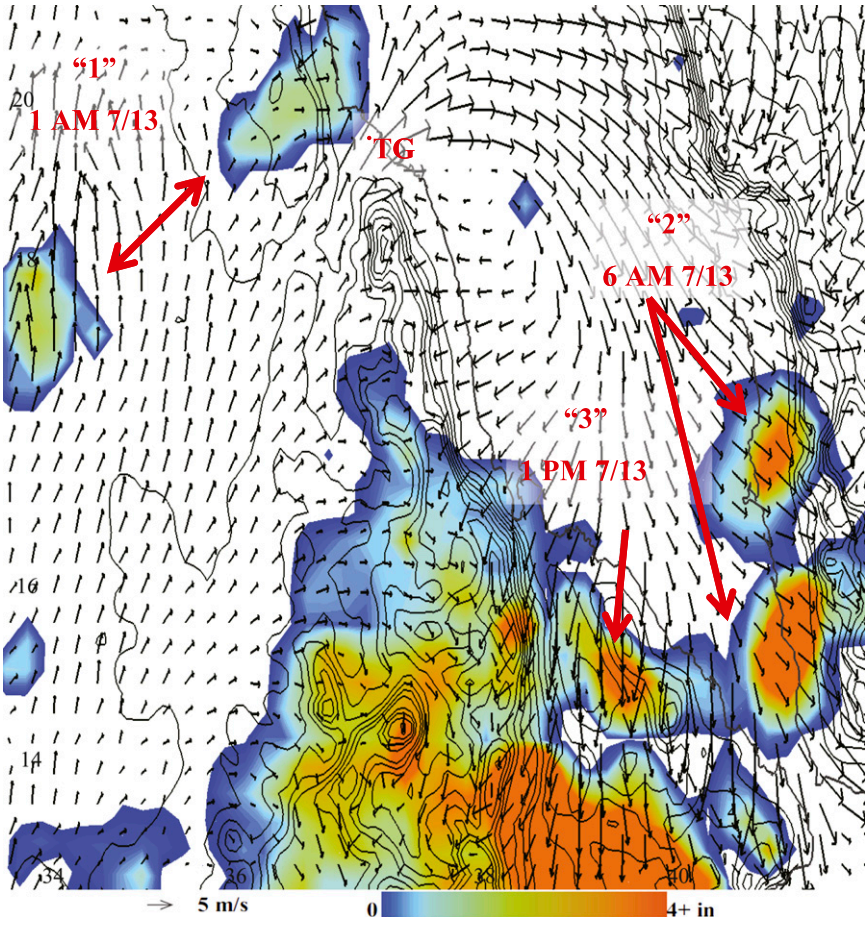

FIG. 14. WRF Model–simulated 10-m wind vectors at 1300 LST 13 July, overlaying solid contours of topography (259 m interval) and color contours of TRMM satellite measurements of cumulative precipitation (in.; 1 in. ≈ 2.54 cm) between 1500 LST 12 July and 1500 LST 13 July. Location of the MCC observed at the entrance of the Tokar Gap during the jet onset on 12 July is marked as system 1. Locations of MCC-induced precipitation observed in the downstream path of the TGJ (and its return flow) along the Arabian coast and the African highland/Afar basin region are marked as systems 2 and 3 respectively.

convective complexes (MCCs). The downwind extension of the Tokar jet flow contributes a moist inland flow that may play a role in regional MCC development on both sides of the Red Sea. This process would be consistent with the TRMM satellite observations of MCCs/precipitation (Fig. 14) during the extreme jet event on 12–13 July 2008. In the overlay of satellite rainfall observations and WRF Model 10-m wind vectors during the full development of the jet (1300 LST 13 July), rainfall contributed by the MCC (system 1) formed at the entrance of the TG during the jet onset (as seen in in the downburst shown in Fig. 9 as well) was positioned just to the northwest of the TG as the system moved northwestward. Development of MCCs with precipitation in the downwind extension of the TGJ was also apparent and consistent with Tomasi's (1984) observation of increases in precipitable water in the southern Red Sea region. In particular, a well-defined MCC was observed downstream along the Arabian coast (system 2) where the TGJ flow encountered major topographic elements on the southern Arabian Peninsula (initially at 0600 LST). Within the return flow of the TGJ toward the African coast (initially 1300 LST), increased precipitation coinciding with MCC development (system 3) and intensification was seen as the flow reached inland within the Afar basin.

7. Summary and conclusions

We have presented an investigation of a summertime coastal gap wind, the Tokar Gap jet, and its possible impacts across the EARSAP region. Through the use of

high-resolution WRF Model simulations over an 8-day period, it was shown that the TGJ is much more than an expression of the local land/sea breeze cycle of the Red Sea. Rather, the occurrence of the TGJ is tied to larger-scale dynamics due to the Tokar Gap's unique proximity to the summertime northward excursion of the ITCZ and resulting diurnal incursion of the southerly Indian Ocean monsoon winds into the African continent. We also find that, during the 8-day period of study, the TGJ was a conduit of significant atmospheric moisture transport with possible bearing upon regional rainfall.

WRF Model simulations demonstrated that during the period studied, the monsoon winds over the EARSAP region behave much like a large-scale sea breeze, in that winds are drawn from the Indian Ocean through the East African interior as a heat low intensifies over the Sahara/Sahel region where the surface ITCZ front is found. The moist/cool marine air of the monsoons progresses inland in the manner of a gravity current or sea breeze front, undercutting the dry/warm continental air in the process. In the case of the two strong events, it was this advancing "monsoon front," and not the local Red Sea land breeze, that triggered the TGJ and secondary jets. The simulated monsoons were channeled toward the ITCZ and TG by prominent topographic elements in the region including the Turkana valley and the East African highlands. In the model analyses and Lagrangian trajectories, it was seen that the principal monsoon flow to the TG emerged north of the Turkana valley between the EAH and EH, in which a year-round low-level jet is maintained.

Downstream, the TGJ was modulated by the local land–sea breeze cycle. In the vicinity of the TG, model sea breezes developed in late afternoon, creating onshore flow that typically ranged from 3 to 8 $m\,s^{-1}$ and were sustained for 2–6 h. The local sea breeze contributed to the attenuation of the outflowing gap winds, reducing and eventually reversing the flow within the TG. A land breeze was generally observed much later in the evening, typically occurring around 2200 LST. This feature was frequently seen as precursor to the TGJ, leading its development by 1–4 h.

Two case studies of strong TGJ events in July 2008 demonstrated the interplay of upstream and downstream influences on the gap wind jet. The first of these was on 12 July 2008 and marked the most extreme TGJ event observed that summer. Winds during this event were sustained above 20 $m\,s^{-1}$ for ~17 h with a maximum velocity of 26 $m\,s^{-1}$, achieved between the surface and 300 m in altitude. The second case study was more typical of strong events observed in the TG, with the jet being sustained for 10 h and peak winds reaching 22 $m\,s^{-1}$. In each TGJ event, the gap winds executed a broad, anticyclonic turn, with radius of curvature close to the inertial radius (about 200 km), resulting in a path that veered east and then southeastward as it passed over the southern Red Sea. This curvature was consistent with a return flow toward the Red Sea Hills, the Afar basin, and the EH/EAH region. Large elevations in the latent heat fluxes (300–800 $W\,m^{-2}$) were also evaluated immediately downstream of the TGJ.

Based on an analysis of the vertically integrated horizontal moisture fluxes, it was seen that the TGJ played a prominent role in the atmospheric moisture transport into the central and southern Red Sea. Over the course of a week-long simulation of gap jet events, the TGJ contributed nearly 3 times as much moisture as the prevailing winds from the northwest, which carried moisture from the northern Red Sea and eastern Mediterranean Sea. It was seen that TGJ events appeared to induce transport of moisture from southern Red Sea across the Saudi Arabian coastline, providing a possible source of occasional rainfall there. In fact, the pulses of high moisture flux due to the gap jet activity on the western Red Sea coast were strongly correlated with landward moisture fluxes across the Saudi coast, with the gap winds leading the fluxes by 7 h. This suggests that the timing and strength of the moist onshore winds at the Saudi coast is strongly influenced by the Tokar jet.

Possible influences of the significant moisture transport achieved by the TGJ (and the associated return flow over the Red Sea) may include the development of mesoscale convective complexes downstream. WRF Model simulations and TRMM satellite observations confirmed that MCCs were generated in the path of the jet over elevated terrain on the Saudi coast, as well as above the topographic elements surrounding the Afar basin along the African side. The transport of moisture and dust by the TGJ across the Arabian coast, and the consequences for Arabian climate, point to a process that does not arise in connection with coastal jets that empty out over "half plane" oceans.

We have suggested a possible link between the TGJ and regional MCCs. Are there links to processes extending beyond the EARSAP region? As Gray (1990) first established, there exists a strong relationship between western Sahelian rainfall and concurrent intense tropical cyclone activity across the North Atlantic Ocean. Landsea et al. (1992) provided an extension of this finding with the analysis of an ~100-yr data record, finding that the correlation was strongest for intense landfalling storms reaching the Atlantic coast of North America and weakest for storms entering the Gulf of Mexico. Contemporary studies have expanded upon these findings and centered on underlying physical mechanisms of this relationship that manifest farther east in the EARSAP region. Specifically, Hill and Lin (2003) established that thunderstorms

or MCCs spawned in the highlands of East Africa were the origins of Hurricane Alberto. In this case, the MCCs responsible for East African rainfall developed sufficient organization (convection and rotation) to be sustained and were advected westward by the African equatorial jet. True tropical cyclogenesis followed their arrival in the tropical Atlantic, where intensification and further development evolved to hurricane levels. Similar cases for the evolution of hurricanes from East African MCCs have been made for Hurricane Isabel (Wu et al. 2006) and Hurricane Sandy (NASA-JPL 2012). Further studies of this kind and efforts to determine a link between MCCs, the TGJ, and impacts over greater ranges would benefit greatly from additional observations. While present satellite wind instruments can resolve the TGJ and wind flow over the Red Sea, missions such as soon to be launched Cyclone Global Navigation Satellite System (CYGNSS) promise sea surface wind observations with greatly increased coverage in space in time for tropical phenomena, which may prove suitable for such questions.

It is hoped that future works building on this study will evaluate the upwind influences as well as the downwind impacts of the TGJ over longer time records. As the role of the monsoon front figures prominently in the jet events shown here, such efforts would benefit from an analysis of ties between the TGJ and the active/break periods of the Indian Ocean monsoons in summer. This would include consideration of the monsoon-influenced Somali jet to the southeast, which has established ties to summer rainfall patterns over the Greater Horn of Africa (Riddle and Cook 2008). A similar exploration of the South Atlantic's influences upon the TGJ would also be interesting. In this study, a small percentage of simulated back trajectories consistently traced back through the Congo River basin and toward the Gulf of Guinea on the West African side. Sun et al. (1999) found similar instances of "Congo moist air" originating from the SHH and influencing the flow in the Turkana/East African region in regional climate simulations. An examination of both Atlantic and Indian Ocean influences upon the TG and the TGJ variability over decadal time scales with attention to established climate signals would do much more to clarify its role in the global climate system.

Acknowledgments. This work was supported by a grant from the King Abdullah University of Science and Technology (KAUST) as well as National Science Foundation Grant OCE0927017 and from DOD (MURI) Grant N000141110087, administered by the Office of Naval Research. The authors would also like to thank Jason Albright, Caroline Ummenhofer, Tom Farrar, Xujing Jia Davis, Paolo Luzzatto-Fegiz, Ping Zhai, and three anonymous reviewers for helpful discussions during the course of the work.

REFERENCES

Bastin, S., and Coauthors, 2006: On the interaction between sea breeze and summer mistral at the exit of the Rhône Valley. *Mon. Wea. Rev.,* **134,** 1647–1668, doi:10.1175/MWR3116.1.

Bergamasco, A., and M. Gačić, 1996: Baroclinic response of the Adriatic Sea to an episode of bora wind. *J. Phys. Oceanogr.,* **26,** 1354–1369, doi:10.1175/1520-0485(1996)026<1354:BROTAS>2.0.CO;2.

Carlson, T. N., and F. E. Boland, 1978: Analysis of urban–rural canopy using a surface heat flux/temperature model. *J. Appl. Meteor.,* **17,** 998–1013, doi:10.1175/1520-0450(1978)017<0998:AOURCU>2.0.CO;2.

Chakraborty, A., S. K. Behera, M. Mujumdar, R. Ohba, and T. Yamagata, 2006: Diagnosis of tropospheric moisture over Saudi Arabia and influences of IOD and ENSO. *Mon. Wea. Rev.,* **134,** 598–617, doi:10.1175/MWR3085.1.

Chang, C. P., 2004: *East Asian Monsoon.* World Scientific Series on Asia-Pacific Weather and Climate, Vol. 2, World Scientific, 370 pp.

Chelton, D. B., M. H. Freilich, and S. K. Esbensen, 2000: Satellite observations of the wind jets off the Pacific coast of Central America. Part I: Case studies and statistical characteristics. *Mon. Wea. Rev.,* **128,** 1993–2018, doi:10.1175/1520-0493(2000)128<1993:SOOTWJ>2.0.CO;2.

Draxl, C., A. N. Hahmann, A. Peña, and G. Giebel, 2014: Evaluating winds and vertical wind shear from Weather Research and Forecasting model forecasts using seven planetary boundary layer schemes. *Wind Energy,* **17,** 39–55, doi:10.1002/we.1555.

Gray, W. M., 1990: Strong association between West African rainfall and U.S. landfall of intense hurricanes. *Science,* **249,** 1251–1256, doi:10.1126/science.249.4974.1251.

Griffiths, J. F., Ed., 1972: Ethiopian highlands. *Climates of Africa,* World Survey of Climatology, Vol. 10, Elsevier, 369–388.

Hickey, B., and A. S. Goudie, 2007: The use of TOMS and MODIS to identify dust storm source areas: The Tokar delta (Sudan) and the Seistan basin (south west Asia). *Geomorphological Variations,* A. S. Goudie and J. Kalvoda, Eds., P3K, 37–57.

Hill, C. M., and Y.-L. Lin, 2003: Initiation of a mesoscale convective complex over the Ethiopian highlands preceding the genesis of Hurricane Alberto (2000). *Geophys. Res. Lett.,* **30,** 1232, doi:10.1029/2002GL016655.

Hughes, M., and A. Hall, 2010: Local and synoptic mechanisms causing Southern California's Santa Ana winds. *Climate Dyn.,* **34,** 847–857, doi:10.1007/s00382-009-0650-4.

Jiang, H., J. T. Farrar, R. C. Beardsley, R. Chen, and C. Chen, 2009: Zonal surface wind jets across the Red Sea due to mountain gap forcing along both sides of the Red Sea. *Geophys. Res. Lett.,* **36,** L19605, doi:10.1029/2009GL040008.

Karnauskas, K. B., R. Seager, A. Giannini, and A. J. Busalacchi, 2013: A simple mechanism for the climatological midsummer drought along the Pacific coast of Central America. *Atmósfera,* **26,** 261–281, doi:10.1016/S0187-6236(13)71075-0.

Kinuthia, J. H., and G. C. Asnani, 1982: A newly found jet in North Kenya (Turkana Channel). *Mon. Wea. Rev.,* **110,** 1722–1728, doi:10.1175/1520-0493(1982)110<1722:ANFJIN>2.0.CO;2.

Landsea, C. W., W. M. Gray, P. W. Mielke Jr., and K. J. Berry, 1992: Long-term variations of western Sahelian monsoon rainfall and

intense U.S. landfalling hurricanes. *J. Climate,* **5,** 1528–1534, doi:10.1175/1520-0442(1992)005<1528:LTVOWS>2.0.CO;2.

Liu, J., J. A. Curry, C. A. Clayson, and M. A. Bourassa, 2011: High-resolution satellite surface latent heat fluxes in North Atlantic hurricanes. *Mon. Wea. Rev.,* **139,** 2735–2747, doi:10.1175/2011MWR3548.1.

Magaña, V., J. A. Amador, and S. Medina, 1999: The mid-summer drought over Mexico and Central America. *J. Climate,* **12,** 1577–1588, doi:10.1175/1520-0442(1999)012<1577:TMDOMA>2.0.CO;2.

Pedgley, D. E., 1974: An outline of the weather and climate of the Red Sea. *L'Oceanographie Physique de la Mer Rouge: Symp. de l'Association International des Sciences Physiques de l'Océan,* Paris, France, UNESCO, 9–27.

Ramaswamy, C., 1962: Breaks in the Indian summer monsoon as a phenomenon of interaction between the easterly and the subtropical westerly jet streams. *Tellus,* **14A,** 337–349, doi:10.1111/j.2153-3490.1962.tb01346.x.

Ramel, R., H. Gallée, and C. Messager, 2006: On the northward shift of the West African monsoon. *Climate Dyn.,* **26,** 429–440, doi:10.1007/s00382-005-0093-5.

Reed, T. R., 1931: Gap winds in the Strait of Juan de Fuca. *Mon. Wea. Rev.,* **59,** 373–376, doi:10.1175/1520-0493(1931)59<373:GWOTSO>2.0.CO;2.

Riddle, E. E., and K. H. Cook, 2008: Abrupt rainfall transitions over the Greater Horn of Africa: Observations and regional model simulations. *J. Geophys. Res.,* **113,** D15109, doi:10.1029/2007JD009202.

Romero-Centeno, R., J. Zavala-Hidalgo, and G. B. Raga, 2007: Mid-summer gap winds and low-level circulation over the eastern tropical Pacific. *J. Climate,* **20,** 3768–3784, doi:10.1175/JCLI4220.1.

Skamarock, W. C., and Coauthors, 2008: A description of the Advanced Research WRF version 3. NCAR Tech. Note NCAR/TN-475+STR, 113 pp. [Available online at http://www2.mmm.ucar.edu/wrf/users/docs/arw_v3.pdf.]

Slingo, J., H. Spencer, B. Hoskins, P. Berrisford, and E. Black, 2005: The meteorology of the western Indian Ocean, and the influence of the East African highlands. *Philos. Trans. Roy. Soc. London,* **363A,** 25–42, doi:10.1098/rsta.2004.1473.

Steedman, R. A., and Y. Ashour, 1976: Sea breezes over north-west Arabia. *Tellus,* **28A,** 299–306, doi:10.1111/j.2153-3490.1976.tb00679.x.

Steenburgh, W. J., D. M. Schultz, and B. A. Colle, 1998: The structure and evolution of gap outflow over the Gulf of Tehuantepec, Mexico. *Mon. Wea. Rev.,* **126,** 2673–2691, doi:10.1175/1520-0493(1998)126<2673:TSAEOG>2.0.CO;2.

Sultan, B., and S. Janicot, 2003: The West African monsoon dynamics. Part II: The "preonset" and "onset" of the summer monsoon. *J. Climate,* **16,** 3407–3427, doi:10.1175/1520-0442(2003)016<3407:TWAMDP>2.0.CO;2.

Sun, F., and J.-Y. Yu, 2006: Impacts of Central America gap winds on the SST annual cycle in the eastern Pacific warm pool. *Geophys. Res. Lett.,* **33,** L06710, doi:10.1029/2005GL024700.

Sun, L., F. H. M. Semazzi, F. Giorgi, and L. J. Ogallo, 1999: Application of the NCAR regional climate model to eastern Africa. Part I: Simulations of the short rains of 1988. *J. Geophys. Res.,* **104,** 6529–6548, doi:10.1029/1998JD200051.

Talley, L. D., G. L. Pickard, W. J. Emery, and J. H. Swift, 2011: *Descriptive Physical Oceanography: An Introduction.* 6th ed. Academic Press, 560 pp.

Thiébaux, J., E. Rogers, W. Wang, and B. Katz, 2003: A new high-resolution blended real-time global sea surface temperature analysis. *Bull. Amer. Meteor. Soc.,* **84,** 645–656, doi:10.1175/BAMS-84-5-645.

Tomasi, C., 1984: Vertical distribution features of atmospheric water vapor in the Mediterranean, Red Sea, and Indian Ocean. *J. Geophys. Res.,* **89,** 2563–2566, doi:10.1029/JD089iD02p02563.

Viste, E., and A. Sorteberg, 2013a: Moisture transport into the Ethiopian highlands. *Int. J. Climatol.,* **33,** 249–263, doi:10.1002/joc.3409.

——, and ——, 2013b: The effect of moisture transport variability on Ethiopian summer precipitation. *Int. J. Climatol.,* **33,** 3106–3123, doi:10.1002/joc.3566.

Webster, P. J., V. O. Magaña, T. N. Palmer, J. Shukla, R. A. Tomas, M. Yanai, and T. Yasunari, 1998: Monsoons: Processes, predictability, and the prospects for prediction. *J. Geophys. Res.,* **103,** 14 451–14 510, doi:10.1029/97JC02719.

Wu, L., S. A. Braun, J. J. Qu, and X. Hao, 2006: Simulating the formation of Hurricane Isabel (2003) with AIRS data. *Geophys. Res. Lett.,* **33,** L04804, doi:10.1029/2005GL024665.

Xie, S.-P., H. Xu, W. S. Kessler, and M. Nonaka, 2005: Air–sea interaction over the eastern Pacific warm pool: Gap winds, thermocline dome, and atmospheric convection. *J. Climate,* **18,** 5–20, doi:10.1175/JCLI-3249.1.

Xu, H., S.-P. Xie, Y. Wang, and R. J. Small, 2005: Effects of Central American mountains on the eastern Pacific winter ITCZ and moisture transport. *J. Climate,* **18,** 3856–3873, doi:10.1175/JCLI3497.1.

Zhai, P., and A. S. Bower, 2013: The response of the Red Sea to a strong wind jet near the Tokar Gap in summer. *J. Geophys. Res. Oceans,* **118,** 422–434, doi:10.1029/2012JC008444.

Zhang, D.-L., L. Tian, and M.-J. Yang, 2011: Genesis of Typhoon Nari (2001) from a mesoscale convective system. *J. Geophys. Res.,* **116,** D23104, doi:10.1029/2011JD016640.